Check for updates

Small Methods

small methods
www.small-methods.com

RESEARCH ARTICLE OPEN ACCESS

One-Step Electrosynthesis of Polyoxometalate-Based Organic–Inorganic Hybrid Polymers and Their Confinement in Vertically Oriented Mesoporous Silica

Odilon Wamba-Tchio[1,2] | Alain Walcarius[1] | Israël Mbomekallé[2] | Neus Vilà[1,3]

[1]Université de Lorraine, CNRS, LCPME, Villers-lès-Nancy, France | [2]Université Paris Saclay CNRS, Institut De Chimie Physique, Orsay, France | [3]Universitat Autònoma de Barcelona, Departament de Química, Bellaterra, Spain

Correspondence: Israël Mbomekallé (israel.mbomekalle@universite-paris-saclay.fr) | Neus Vilà (neus.vila.cusco@uab.cat)

Received: 27 April 2026 | **Revised:** 10 June 2026 | **Accepted:** 25 June 2026

Keywords: bifunctional POM-aniline monomers | electrocatalysis | electropolymerization | polyoxometalate-based nanowires | vertically-oriented mesoporous silica films

ABSTRACT

The development of organic–inorganic hybrid polyoxometalates (POMs) covalently linked to conducting polymers is an effective strategy to preserve their electrochemical accessibility upon immobilization. However, conventional approaches typically involve multistep syntheses, resulting in low POM loading and limited nanoscale control. Here, we report a one-step electrosynthetic approach to generate a POM-rich conducting polymer via electropolymerization of a bifunctional precursor, PW_{11}-$(ANI)_2$, bearing two aniline moieties. Electropolymerization is first demonstrated on bare indium–tin oxide (ITO) electrodes and then extended to the formation of poly(PW_{11}-ANI) nanofilaments confined within vertically aligned mesoporous silica films (VMSF). The process is initiated by electrochemical oxidation of the aniline groups, generating radical cations that couple to form the hybrid polymer, as evidenced by the progressive growth of reversible POM-centered voltammetric signals. The resulting surface-confined films exhibit good adhesion, further enhanced by a preliminary electrografting step using the monodiazonium derivative PW_{11}-(ANI)(diaz). Both films and nanoconfined structures are electroactive and display electrocatalytic activity toward nitrite reduction, which is enhanced under confinement. These results demonstrate the potential of aniline-functionalized POMs as versatile building blocks for electroactive hybrid materials in sensing, electrochromic, and energy storage applications.

1 | Introduction

Conducting polymers have evolved from traditional bulk materials into advanced systems with tunable molecular architectures, enabling precise control over electronic properties [1–3]. The design of efficient and robust electroactive functionalized polymeric materials is central to advancing technologies for energy conversion and environmental remediation. Among the various molecular candidates for functionalization, polyoxometalates (POMs), discrete metal–oxygen cluster anions, have garnered significant attention owing to their rich redox chemistry, structural versatility, and ability to mediate multi-electron transfer reactions [4–9]. However, their practical use for electroanalytical purposes (e.g., in electrochromic devices, for electrocatalysis, photoelectrochemistry, or electrochemical energy storage) remains limited by critical issues such as solubility, leaching, and poor recyclability in homogeneous systems [10–18].

Immobilizing POMs within conductive polymer matrices has proven to be a promising strategy to overcome the limitations related to the poor processability of the POMs, thus offering solid-state supports with increased durability and efficient electron

This is an open access article under the terms of the Creative Commons Attribution-NonCommercial-NoDerivs License, which permits use and distribution in any medium, provided the original work is properly cited, the use is non-commercial and no modifications or adaptations are made.
© 2026 The Author(s). *Small Methods* published by Wiley-VCH GmbH

transfer [19, 20]. Traditionally, POMs have been incorporated as counter-anions during the electrochemical synthesis of conducting polymers, particularly under oxidative electropolymerization conditions [21, 22], or via physical blending/entrapment [23]. The anionic nature of these species ensures electrostatic stabilization of the positively charged polymer backbone; independently, their redox activity introduces functional properties, including ion-transport regulation and redox-switchable behavior. Despite these advantages, the use of POMs as dopant is associated with key limitations, including limited spatial control, potential leaching, and the lack of permanent electronic coupling to the polymer framework, which can result in inefficient charge transport and partial electrochemical inaccessibility of the POMs.

A breakthrough came about, thanks to the development of organic–inorganic hybrid POMs by covalently linking functional organic groups directly to the polyoxometalate core [24–26]. This molecular-level design enables tailored solubility, interfacial interactions, and electronic communication between the inorganic cluster and the organic functionality. In addition, hybrids bearing electropolymerizable, photoactive, or redox-active groups allow POM units to be permanently integrated into polymer backbones, preventing anion loss and enhancing the stability and functionality of the resulting hybrid films. Another strategy relies on designing supramolecular assemblies made of organically-functionalized POMs [27, 28]. Such systems bridge molecular and macroscopic scales, providing access to electroactive materials with tunable conductivity, catalytic activity, and structural robustness. Yet, the function-directed rational design of covalently modified POMs, while keeping their whole electrochemical accessibility when immobilized, remains highly challenging [29, 30].

A promising approach to immobilize durably high contents of electrochemically accessible POMs onto an electrode surface would be their covalent bonding to a conductive polymer matrix. A first attempt for electrochemically generated polymer films incorporating POMs covalently tethered to a pyrrole (Py) unit has been reported [31]. In that study, however, Lindqvist-type POMs bearing only a single electropolymerizable pyrrole required the addition of pyrrole as a comonomer in the synthesis medium to achieve film formation, yielding an organic–inorganic hybrid polymer in which the POM units were covalently integrated into the polymer backbone.

In this work, we report the first example of the electropolymerization of a hybrid organic–inorganic POM bearing two intrinsic electropolymerizable units, PW_{11}-$(ANI)_2$ (Scheme 1A), which is likely to condense and polymerize without the need of additional monomers. Unlike prior strategies in which POMs act mainly as anionic dopants, the aniline groups in PW_{11}-$(ANI)_2$ are covalently attached to the cluster and serve as the active polymerization sites. Electropolymerization of this molecular precursor affords the hybrid polymer poly(PW_{11}-ANI) (Scheme 1B), which can be directly deposited on bare ITO electrodes or as nanofilaments confined within vertically aligned mesoporous silica thin films. This approach combines the advantages of molecular-level POM design with nanoscale confinement, offering a new paradigm for constructing robust, electroactive hybrid materials for electrochemical applications. The experimental section (with Figures S1–S3) is detailed in the Supporting Information section.

2 | Results and Discussion

2.1 | Poly(PW_{11}-ANI) on ITO Electrode

2.1.1 | Electrochemical Behavior and Evidence of the Direct Electropolymerization Process of PW_{11}-$(ANI)_2$ on Bare ITO

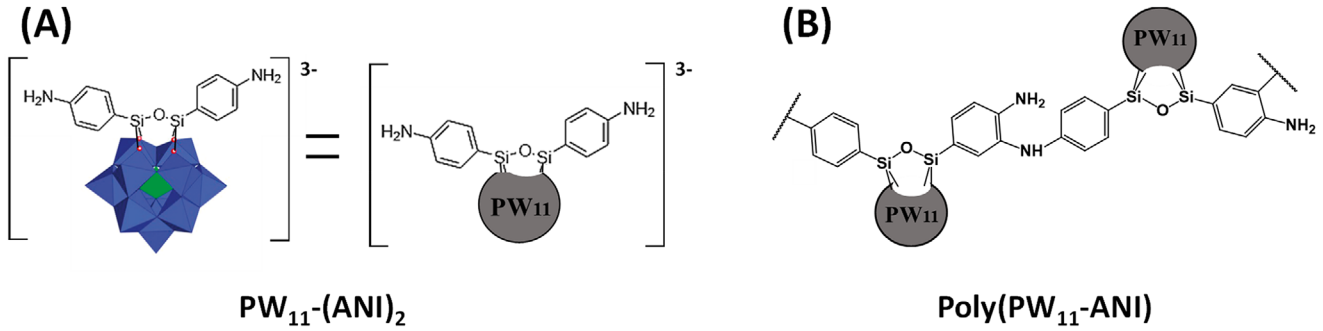
Figure 1A shows a typical cyclic voltammogram recorded for the organic–inorganic hybrid precursor PW_{11}-$(ANI)_2$, in acetonitrile (ACN) solution containing 0.1 M n-Bu_4NClO_4 as supporting electrolyte, on an ITO electrode. In this medium, during an initial cathodic potential scan from 0 V to –1.8 V versus Ag/AgCl, **PW_{11}-$(ANI)_2$** exhibits three well-defined, single-electron reversible redox waves at $\boldsymbol{E_1^0}$ **= -0.39 V**, $\boldsymbol{E_2^0}$ **= -0.92 V**, and $\boldsymbol{E_3^0}$ **= -1.48 V** versus **Ag/AgCl**, which correspond to the successive reduction of the tungsten centers within the Keggin-type polyoxometalate (POM) core [32]. In addition, a quasi-reversible anodic process is observed at E_{pa} = +1.09 V vs. Ag/AgCl during the reverse anodic scan (as the potential is swept from -1.8 V up to +1.3 V). This signal, which does not exist for nonfunctionalized PW_{11} is attributed to the oxidation of the -$PhNH_2$ moieties of PW_{11}-$(ANI)_2$.

It should be noted that acetonitrile (with n-Bu_4NClO_4 electrolyte) was initially employed as a solvent for CV experiments (Figure 1A). In this medium, no evidence of electropolymerization was observed during multi-sweep CV (see Figure SI4), likely due to the lack of protons necessary to trigger the effective anodic oxidation of the aminophenyl groups and their subsequent polycondensation. In this sense, it is well-known that the electrochemical polymerization of aniline and aniline derivatives is typically performed in strongly acidic aqueous electrolytes, following a widely accepted mechanism that involves the formation of an anilinium radical cation through the oxidation of aniline at the electrode [33]. So that, further electrochemical investigations with PW_{11}-$(ANI)_2$ were conducted in an acidic environment composed of 0.2 M $HClO_4$ in ACN (Figure 1B). In this medium, focusing on the potential window characteristic of cathodic signal associated with the first reduction of the tungsten centers, one can clearly see a progressive increase in the peak current intensity with successive scans (I_{pc} increasing from -107 µA for the first scan to -295 µA for the 100th one), which is indicative of an effective electropolymerization to form poly(PW_{11}-ANI). Notably, this increase occurred only after the oxidation of the —$PhNH_2$ moieties, indicating a correlation between their oxidation and the electropolymerization process. The redox behavior indicates electronic communication between the POM and aniline units, suggesting partial delocalization of charge and possible intramolecular electron transfer. A more detailed analysis of the electrochemical behavior in the anodic region is provided hereafter.

2.1.2 | Mechanistic Insights in the Electrochemical Polymerization Mechanism of PW_{11}-$(ANI)_2$ on Bare ITO

As previously noted, the electropolymerization seems to occurs only after the electrochemical oxidation of the —$PhNH_2$ moieties present in the PW_{11}-$(ANI)_2$ structure. Accordingly, no evidence

23669608, 2026, 15, Downloaded from https://onlinelibrary.wiley.com/doi/10.1002/smtd.70834 by Spanish Cochrane National Provision (Ministerio de Sanidad), Wiley Online Library on [04/11/2026]. See the Terms and Conditions (https://onlinelibrary.wiley.com/terms-and-conditions) on Wiley Online Library for rules of use; OA articles are governed by the applicable Creative Commons License



SCHEME 1 | Chemical structures of (A) the monomer **PW_{11}-$(ANI)_2$** and (B) the corresponding polymer **poly(PW_{11}-ANI)**. Counter cations are omitted.

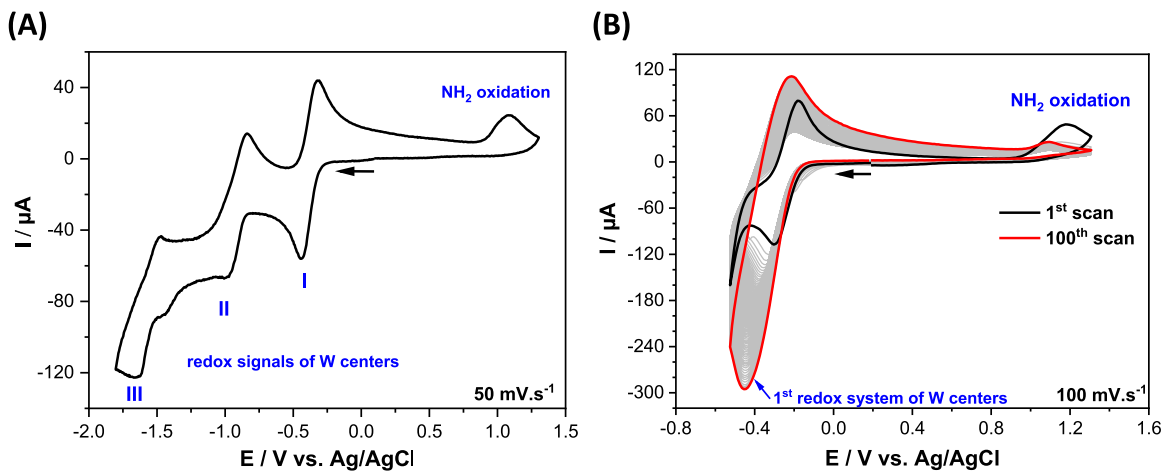


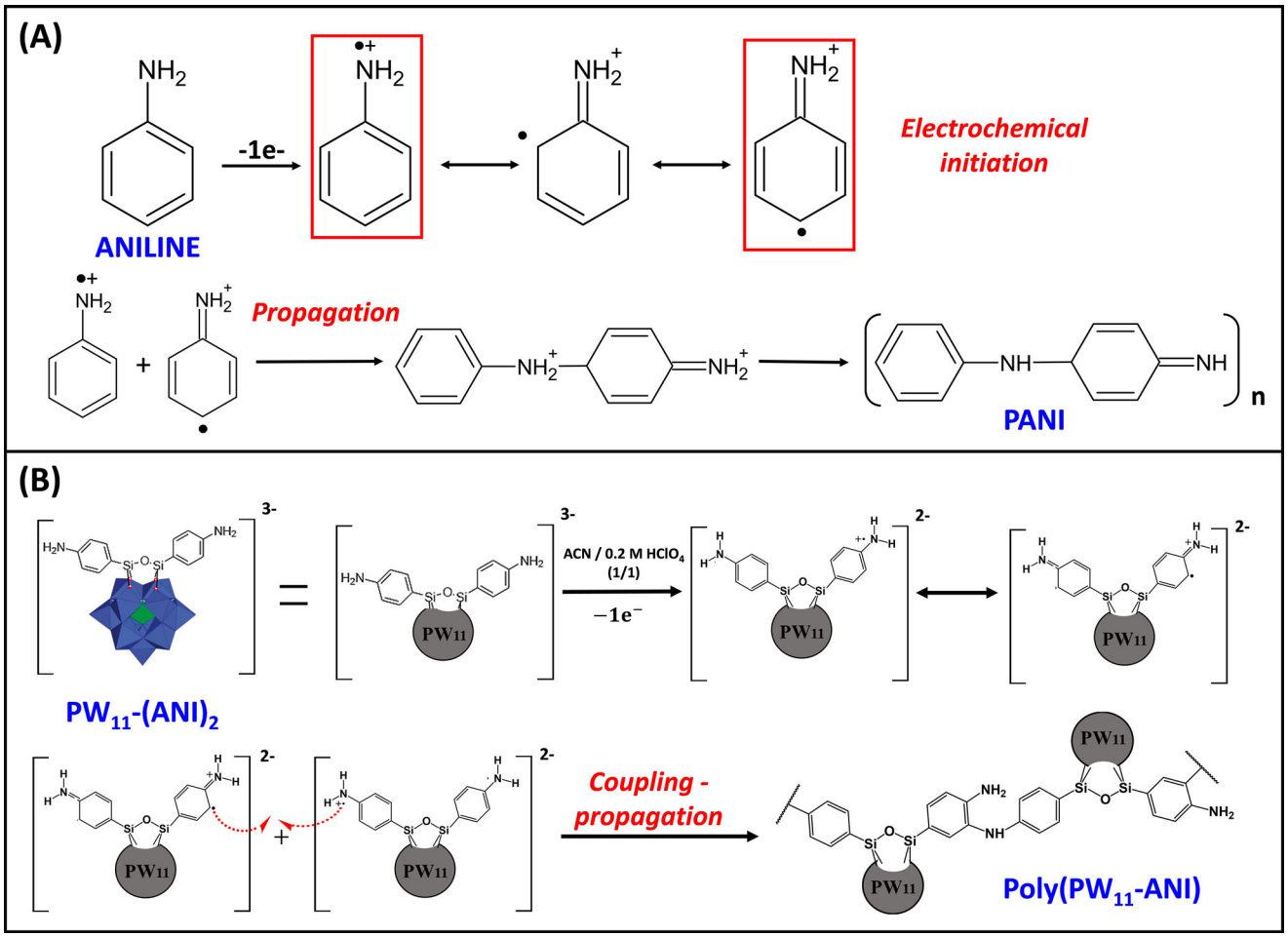
FIGURE 1 | Comparison of the electrochemical behavior observed by cyclic voltammetry of (A) 0.5 mM PW_{11}-$(ANI)_2$ in acetonitrile + 0.1 M *n*-Bu_4NClO_4 at 50 mV.s^{-1} and (B) 2.5 mM PW_{11}-$(ANI)_2$ in acetonitrile / aqueous 0.2 M $HClO_4$ (1/1 vol/vol) at 100 mV.s^{-1}. Working electrode: bare ITO.

of electropolymerization is observed when the applied potential window is limited to the cathodic region, where only the reduction of the tungsten centers takes place (see Figure SI5), confirming that the initiation of the electropolymerization process requires the prior oxidation of at least one —$PhNH_2$ group. The oxidative electrochemical polymerization mechanism of aniline is well-established [33]. The electro-generation of polyaniline (PANI) begins with an initiation step involving the formation of the aniline radical cation, which exhibits delocalization of its unpaired electron, giving rise to two possible isomeric forms that participate in the propagation step of aniline electropolymerization (Scheme 2A). Among the possible pathways, the most favorable propagation step involves **C—N coupling** between the radical cation delocalized at the para position and the initial radical cation centered on the nitrogen atom.

Figure 2 compares the electrochemical responses recorded during the electropolymerization of aniline in the anodic region (Figure 2A) and that of the hybrid PW_{11}-$(ANI)_2$ in the same potential window (Figure 2B), as performed in the same medium (ACN + 0.2 M $HClO_4$). Although both systems exhibit analogous features at utmost anodic potentials, the electropolymerization pathway of PW_{11}-$(ANI)_2$ is dictated by its molecular architecture. Upon anodic oxidation, the initial electron transfer generates a nitrogen-centered radical, which subsequently couples with the radical localized at the ortho position of the aromatic ring. In contrast to unsubstituted aniline, the para position is blocked in PW_{11}-$(ANI)_2$, preventing the classical head-to-tail coupling and favoring ortho-oriented polymer growth. This structural constraint ultimately governs the electropolymerization mechanism and the nature of the resulting metallopolymer film, as illustrated in Scheme 2B. It should be noted that, although the predominance of ortho-coupling is strongly supported by steric constraints imposed by the POM moiety and by the acidic conditions of electropolymerization, which limit alternative pathways, direct structural evidence of the coupling mode within the polymer backbone is not available at this stage, and the proposed mechanism should therefore be considered as the most plausible scenario based on indirect experimental observations and chemical reasoning.

During the first anodic scan, the onset of oxidation of pure aniline is observed at approximately +0.85 V, with the current rising up to +1.30 V versus Ag/AgCl (Figure 2A). This irreversible oxidation process corresponds to the formation of aniline radical cations, which rapidly couple to initiate the growth of a polyaniline (PANI) film on the electrode surface. In the subsequent reverse scan, a new cathodic peak emerges at 0.43 V, and in following

23669608, 2026, 15, Downloaded from https://onlinelibrary.wiley.com/doi/10.1002/smtd.70834 by Spanish Cochrane National Provision (Ministerio de Sanidad), Wiley Online Library on [04/11/2026]. See the Terms and Conditions (https://onlinelibrary.wiley.com/terms-and-conditions) on Wiley Online Library for rules of use; OA articles are governed by the applicable Creative Commons License



SCHEME 2 | Illustrative schemes comparing the electropolymerization mechanisms of (A) pure aniline and (B) the POM-aniline PW_{11}-$(ANI)_2$ hybrid.

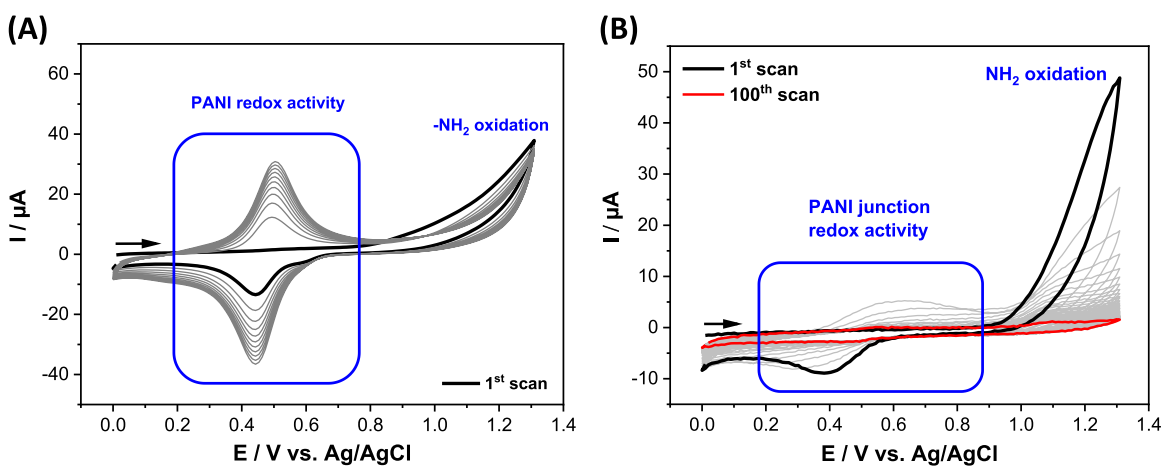


FIGURE 2 | Electropolymerization of (A) pure 1 mM aniline and (B) 2.5 mM PW_{11}-$(ANI)_2$ on ITO electrode in acetonitrile/aqueous 0.2 M $HClO_4$ (1/1 vol/vol) at 100 $mV.s^{-1}$ in the anodic region from 0 V to 1.3 V versus Ag/AgCl.

cycles, an associated anodic peak appears at +0.49 V. The gradual increase in the current of this redox couple reflects the progressive growth of the PANI film and is characteristic of its reversible **doping/dedoping** processes [34].

By contrast, the electrochemical oxidation of the hybrid PW_{11}-$(ANI)_2$ (exhibiting a progressive current increase beginning at approximately +0.90 V and extending to +1.30 V) is consistent with the formation of PANI junctions during the first reverse

23669608, 2026, 15, Downloaded from https://onlinelibrary.wiley.com/doi/10.1002/smtd.70834 by Spanish Cochrane National Provision (Ministerio de Sanidad), Wiley Online Library on [04/11/2026]. See the Terms and Conditions (https://onlinelibrary.wiley.com/terms-and-conditions) on Wiley Online Library for rules of use; OA articles are governed by the applicable Creative Commons License

scan (Figure 2B). Compared with pure PANI, the hybrid displays an attenuated redox response that decreases with the successive CV cycles, likely due to the reduced conductivity imparted by the nonconjugated PW_{11}-$(ANI)_2$ units. These results, associated to previous observations (Figure 1B), confirm the formation of an electroactive poly(PW_{11}-ANI) film with partial electronic communication between the POM and the growing pseudo-PANI network, highlighting its potential for redox-based applications. Although overoxidation of polyaniline-type backbones may occur at high anodic potentials, the continuous increase in current and preservation of well-defined redox features over repeated cycling indicate that film growth remains the dominant process under the present conditions.

In addition, the progressive increase in peak current observed over successive CV cycles (Figure 1B) provides strong evidence for a continuous buildup of electroactive material on the electrode surface. Such behavior is characteristic of electropolymerization processes, where film growth proceeds through repeated oxidation of aniline moieties into radical cations followed by coupling and propagation [35, 36]. In contrast, a process dominated by physical adsorption would be expected to rapidly reach saturation, leading to a stable or decreasing current response after a few cycles. Furthermore, the persistence of the electrochemical signal after rinsing and transfer to blank electrolyte (Figure 5) supports the formation of a stable, surface-confined layer rather than weakly adsorbed species. These observations collectively support a covalent electropolymerization mechanism rather than simple adsorption.

2.1.3 | Electrografting of the PW_{11}-$(ANI)_2$ on Bare ITO via 'In Situ'Generation of the Corresponding Diazonium Salt of PW_{11}-$(ANI)_2$, PW_{11}-(ANI)(Diaz)

Even if direct electropolymerization of PW_{11}-$(ANI)_2$ on bare ITO yielded a robust poly(PW_{11}-ANI) film exhibiting strong adhesion, which remained visibly stable even after ultrasonic treatment, without covalent anchorage to the electrode surface it may suffer from some restricted operational stability upon prolonged use (see discussion in section 3.5). In order to possibly improve the long-term stability of the film-electrode interface, we have evaluated the eventual interest of attaching PW_{11}-$(ANI)_2$ onto the ITO surface prior to performing the electropolymerization. A molecular monolayer of PW_{11}-$(ANI)_2$ was covalently attached to the ITO surface through in-situ electrografting of the corresponding monodiazonium derivative (i.e., PW_{11}-(ANI)(diaz), generated by diazotization of PW_{11}-$(ANI)_2$ with $NOBF_4$) in acetonitrile containing 0.1 M $TBAClO_4$. The cathodic electrografting was performed via four consecutive CV scans between +0.2 V and -0.45 V vs. Ag/AgCl (Figure 3A). The voltammetric response of PW_{11}-(ANI)(diaz) in this medium displays a broad pre-wave centered at -0.1 V versus Ag/AgCl (in addition to the expected reduction of the tungsten centers of the POM), which is attributed to reduction of the diazonium group. This process generates surface-confined aryl radicals that subsequently form covalent bonds with the ITO surface (Scheme 3), as previously reported for other species electrografted on ITO [37–39] or for other POM derivatives on ITO or carbon electrodes [30, 40], for instance.

The electrochemical response of the electrografted layer (Figure 3B) exhibits the characteristic reversible redox couple associated with the tungsten centers of the anchored $[PW_{11}O_{39}]^{7-}$ units. Integration of this signal allowed the surface concentration to be evaluated as $\mathbf{1.9 \times 10^{-11}\ mol{\cdot}cm^{-2}}$, corresponding roughly to the formation of a **monolayer of PW_{11}-$(ANI)_2$**. This measured surface concentration is in the order of magnitude of those reported values for other grafted Keggin-type POMs [43], yet lower than the theoretical limit expected for a closely packed monolayer of these POMs ($\mathbf{9.2 \times 10^{-11}\ mol{\cdot}cm^{-2}}$ if considering that a nonfunctionalized Keggin POM occupies 1.8 nm^2) consistent with the presence of silyl-aminophenyl groups in the present case. Anyway, successful grafting was achieved and the electrochemical response was stable upon multiple CV scans (Figure 3B), confirming the durable immobilization of **PW_{11}-(ANI)**(diaz) onto the electrode surface.

2.1.4 | Electrochemical Polymerization on an PW_{11}-(ANI)(Diaz) Electrografted ITO Surface With PW_{11}-$(ANI)_2$ in Solution

We investigated the influence of a monolayer of PW_{11}-(ANI) electrografted on ITO on the subsequent electrochemical polymerization process, by carried out the electropolymerization in a solution containing 2.5 mM PW_{11}-$(ANI)_2$ in ACN + 0.2 M $HClO_4$ (Figure 4), that is, in the same conditions as used before for bare ITO (Figure 1B). As shown, the presence of a preformed monolayer on the ITO surface exerts only a minor influence on the electropolymerization of PW_{11}-$(ANI)_2$, showing slightly lower cathodic peak currents associated with the reduction of the tungsten centers after 100 cycles (Figure 4A). This can be related to a slightly reduced accessibility to the working electrode induced by the presence of PW_{11}-(ANI) moieties distributed on its surface. Nevertheless, it should be mentioned that by analyzing the first redox system of tungsten centers (first scan) on bare ITO and on bare ITO with a previous electrografted monolayer of PW_{11}-$(ANI)_2$, the difference between anodic and cathodic peak potentials ΔE_p and characteristic potentials are almost identical (0.11 V and 0.10 V as ΔE_p, and -0.248 V and -0.253 V vs. Ag/AgCl as $E°$) indicating quite similar electron transfer kinetics in both cases. However, the presence of the grafted monomer seems to allow reaching the steady state a little faster and in a more regular way (Figure 4B).

2.1.5 | Electrochemical Characterization of Poly(PW_{11}-ANI) Coated on ITO

Figure 5 illustrates the cyclic voltammetry (CV) characterization of poly(PW_{11}-ANI) films that were previously obtained by electropolymerization on ITO electrode. It is worth mentioning that, prior to CV analyses, such coated electrodes were ultrasonicated in acetone for 5 min and rinsed with acetonitrile to remove the poorly-adsorbed oligomers at the electrode surface. Figure 5A shows 50 successive CV scans recorded at 50 $mV.s^{-1}$ in the potential window from 0 to -0.57 V versus Ag/AgCl (corresponding to the first redox system of the POM, W centers), in an acetonitrile solution containing only the supporting electrolyte (0.1 M n-Bu_4NClO_4), for poly(PW_{11}-ANI) films respectively prepared by

23669608, 2026, 15, Downloaded from https://onlinelibrary.wiley.com/doi/10.1002/smtd.70834 by Spanish Cochrane National Provision (Ministerio de Sanidad), Wiley Online Library on [04/11/2026]. See the Terms and Conditions (https://onlinelibrary.wiley.com/terms-and-conditions) on Wiley Online Library for rules of use; OA articles are governed by the applicable Creative Commons License

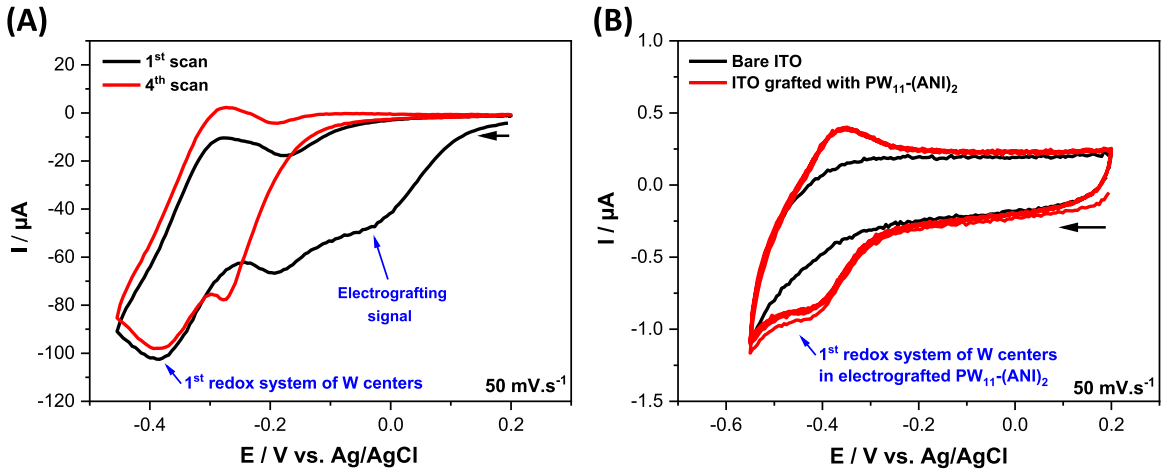
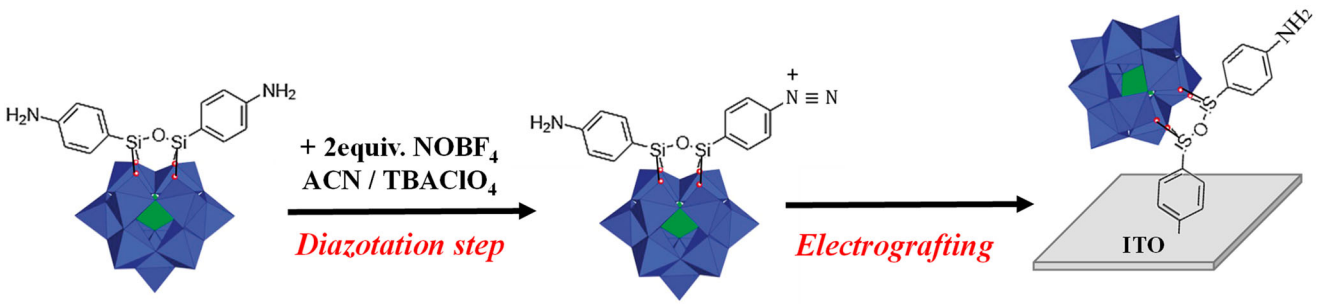


FIGURE 3 | (A) Cyclic voltammograms (first and fourth scans) recorded in 1 mM of PW_{11}-(ANI)(diaz) diazonium cation in ACN + 0.1 M *n*-Bu_4NClO_4, at 50 $mV.s^{-1}$, on bare ITO electrode. (B) Cyclic voltammograms recorded at 50 $mV.s^{-1}$ in ACN + 0.1 M *n*-Bu_4NClO_4 using an ITO electrode surface electrografted with PW_{11}-(ANI)(diaz).



SCHEME 3 | General procedure for in situ generation of the monodiazonium salt **PW_{11}-(ANI)**(diaz) and its subsequent electrografting on ITO surface in organic medium (acetonitrile + 0.1 M $TBAClO_4$).

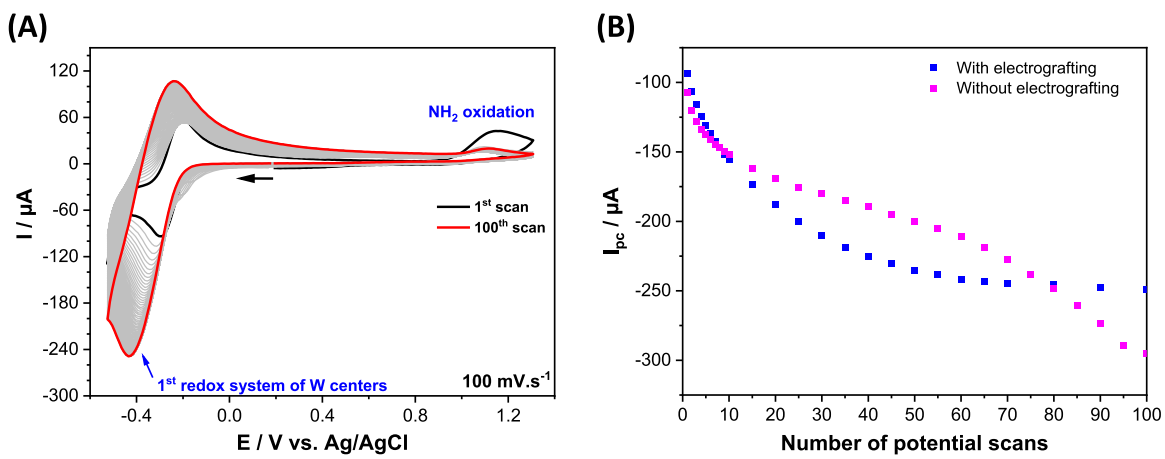


FIGURE 4 | (A) CV curves recorded at 100 $mV.s^{-1}$ during the electropolymerization of 2.5 mM PW_{11}-$(ANI)_2$ in acetonitrile / aqueous 0.2 M $HClO_4$ (1/1 vol/vol) using an ITO electrode modified with a previously electrografted monolayer of PW_{11}-$(ANI)_2$. (B) variation of the cathodic peak currents, I_{pc}, with the number of CV scans (including data previously obtained for the bare ITO as depicted on Figure 1B).

electropolymerization (from a 2.5 mM PW_{11}-$(ANI)_2$ solution) on bare ITO (100 CV scans between -0.52 V and +1.30 V as in Figure 1B (Figure $5A_1$) and between 0 V and +1.30 V as in Figure 2B (Figure $5A_2$)) and on ITO previously electrografted with **PW_{11}-(ANI)**(diaz) between -0.52 V and +1.30 V as in Figure 4A (Figure $5A_3$). In all cases, a reversible current signal is observed around -0.4 V, which is attributed to the first reduction wave of the tungsten centers. Comparison of the first scan (black line)

23669608, 2026, 15, Downloaded from https://onlinelibrary.wiley.com/doi/10.1002/smtd.70834 by Spanish Cochrane National Provision (Ministerio de Sanidad), Wiley Online Library on [04/11/2026]. See the Terms and Conditions (https://onlinelibrary.wiley.com/terms-and-conditions) on Wiley Online Library for rules of use; OA articles are governed by the applicable Creative Commons License

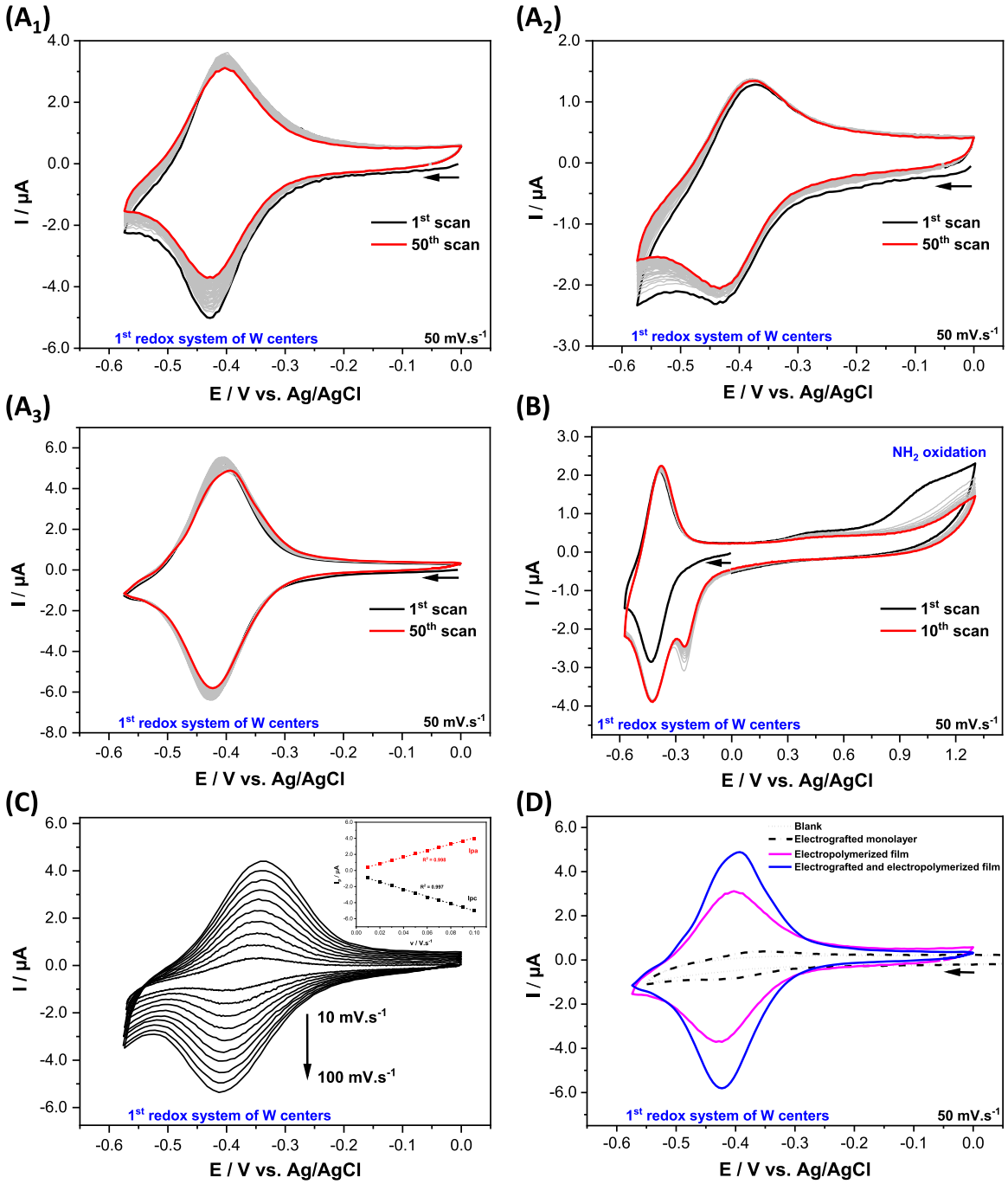


FIGURE 5 | Cyclic voltammetry characterization of poly(PW_{11}-ANI) films on ITO electrodes in ACN + 0.1 M *n*-Bu_4NClO_4: (A), (C), and (D) narrower potential window focusing on the first redox system of the POM (W centers) and (B) broader potential window showing the redox processes of both W centers and electropolymerized aniline moieties. Scan rates are 50 $mV.s^{-1}$ except in (C) where they vary from 10 $mV.s^{-1}$ to 100 $mV.s^{-1}$. Poly(PW_{11}-ANI) films were obtained by electropolymerization between -0.52 V and +1.30 V (A_1,B,C) and 0.00 V and +1.30 V (A_2) on bare ITO electrode, and between -0.52 V and +1.30 V on ITO previously electrografted with **PW_{11}-(ANI)**(diaz) (A_3). Part (D) of the figure compare the CV responses obtained after **PW_{11}-(ANI)**(diaz) electrografting, and after poly(**PW_{11}**-ANI) generation on bare ITO and on electrografted ITO electrodes.

with the fiftieth scan (red line) under identical conditions reveals that the electropolymerized bare ITO surfaces exhibit quite good operational stability, with a ~24% decrease in peak current after repeated cycling for the film electropolymerized between -0.52 V and +1.30 V (Figure 5A_1) and only ~4% decrease for the thinner film prepared between 0 V and +1.30 V (Figure 5A_2), yet with larger cathodic-to-anodic peak separation in the latter case (70 mV, compared to 24 mV in the former case) suggesting better reversibility for the films prepared in wider potential window. Even better operational stability was obtained for the poly(PW_{11}-ANI) film generated between -0.52 V and +1.30 V but on ITO previously electrografted with **PW_{11}-(ANI)**(diaz) for which no noticeable decrease in peak currents were observed between the first and 50th CV scans (Figure 5A_3) while keeping a low cathodic-to-anodic peak separation (23 mV). Compared to the ~24% decrease for the film prepared in the same conditions on bare ITO,

23669608, 2026, 15, Downloaded from https://onlinelibrary.wiley.com/doi/10.1002/smtd.70834 by Spanish Cochrane National Provision (Ministerio de Sanidad), Wiley Online Library on [04/11/2026]. See the Terms and Conditions (https://onlinelibrary.wiley.com/terms-and-conditions) on Wiley Online Library for rules of use; OA articles are governed by the applicable Creative Commons License

this demonstrates the interest of electrografting to improve the long-term stability of poly(PW_{11}-ANI) on the electrode surface. It should be noted that the stability assessment presented here is based on cyclic voltammetry measurements, and that long-term stability under continuous electrolysis conditions, particularly in acidic aqueous media, remains to be investigated.

Figure 5B presents the first (black) and tenth (red) CV scans recorded after stabilization of the cathodic peak current, starting at 0 V, scanning cathodically to -0.6 V, and then reversing anodically to +1.3 V versus Ag/AgCl. As in Figure $5A_1$, a reversible reduction peak associated with the tungsten centers of the $[PW_{11}O_{39}]^{7-}$ units in the poly-(PW_{11}-ANI) film is observed. Upon scanning to anodic potentials up to +1.3 V versus Ag/AgCl, a broad and irreversible anodic peak appears around +1.05 V, which is attributed to the oxidation of the amino groups in the polymer backbone. During the second consecutive cathodic scan, a new irreversible reduction peak appears at **-0.25 V**, which is only observed following the oxidation of the amino groups. The exact origin of this voltammetric feature remains uncertain; however, it may be tentatively attributed to the formation of nonequivalent tungsten centers within the polymer. The prior oxidation of the $-NH_2$ moieties could generate localized positive charges, thereby facilitating the reduction of tungsten centers situated in closer proximity to these functional groups.

A more detailed investigation of the cathodic electrochemical behavior of poly(PW_{11}-ANI) was performed by analyzing the dependence of the peak current on the potential scan rate. In all cases (see an illustrative example in Figure 5C for the same film as in Figure $5A_1$), the first cathodic peak currents attributed to the reduction of tungsten centers increased linearly with the potential scan rate, indicating a thin-layer electrochemical behavior, consistent with the thin film morphology and fast electron transfer within the polymer. The charge transport properties of the film were further evaluated using three redox probes ($[Ru(NH_3)_6]^{3+}$, $[Fe(CN)_6]^{3-}$, and $Fc(MeOH)_2$) on ITO@Poly(PW_{11}-ANI) compared to bare ITO, coupled with electrochemical impedance spectroscopy measurements. The electron transfer kinetic parameters (ΔE, Ipa/Ipc, E_p—$E_{1/2}$) of the cationic probe $[Ru(NH_3)_6]^{3+}$ and the neutral probe $Fc(MeOH)_2$ are comparable on ITO@Poly(PW11-ANI) and on bare ITO, confirming the good conductivity of the deposited metallopolymer (see Figure S6 and Table S1). This conclusion is further supported by EIS measurements, where similar purely diffusional Nyquist diagrams were obtained for bare ITO and ITO@Poly(PW11-ANI), yielding comparable equivalent circuit parameters after fitting with an appropriate electrochemical model (see Figure S7 and Table S2). The electron transfer kinetics of the anionic probe $[Fe(CN)_6]^{3-}$ are however significantly hindered on ITO@Poly(PW_{11}-ANI) compared to bare ITO, which is attributed to electrostatic repulsion between the anionic probe and the highly negatively charged POM units constituting the polymer backbone (see Figure S6).

Figure 5D compares the electrochemical responses of three surfaces: the electrografted monolayer (dashed black line in Figure 5D), the directly electropolymerized bare ITO electrode (solid black line in Figure 5D), and the ITO surface subjected to prior electrografting followed by electropolymerization (solid red line in Figure 5D). Integration of the cathodic responses reveals that direct electropolymerization produces a lower electrochemical signal than the sequential electrografting followed by electropolymerization approach. This behavior is quite unexpected based on the smaller peak currents observed during electropolymerization on electrografted surfaces (compare Figures 4A and 1B) but can be rationalized by the improved adhesion and stability of the polymer when deposited on an electrografted layer upon washing and ultrasonic treatment performed at the end of the electropolymerization process. Integration of this cathodic signal allowed the estimation of surface concentrations in both cases, direct electropolymerization and electropolymerization after electrografting, leading to values of $\mathbf{2.0 \times 10^{-10}\ mol.cm^{-2}}$ and $\mathbf{3.8 \times 10^{-10}\ mol.cm^{-2}}$, respectively. These values are more than one order of magnitude higher than those corresponding to the electrografted monolayer (and also much larger than a dense packing of such POM units on a flat surface [38], confirming the success of the electropolymerization in generating a multilayered poly(PW_{11}-ANI) film with a high content of electrochemically accessible PW_{11} units.

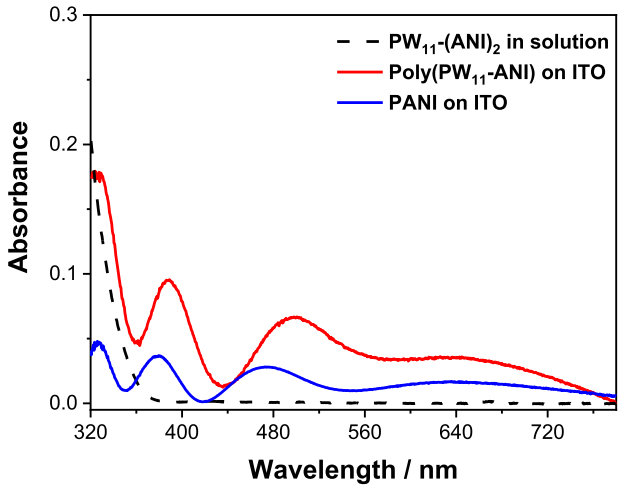


FIGURE 6 | UV–vis absorption spectra of 0.05 mM PW_{11}-$(ANI)_2$ in 0.2 M $HClO_4$-acetonitrile solution (black dotted line), the electropolymerized poly(PW_{11}-ANI) film on ITO (red solid line), and the reference PANI film on ITO (blue solid line).

2.1.6 | Physico-Chemical Characterization of Poly(PW_{11}-ANI)

2.1.6.1 | Optical characterization. The UV–vis absorption spectrum of the electropolymerized poly(PW_{11}-ANI) film on ITO was thoroughly analyzed and compared to those of the monomeric precursor PW_{11}-$(ANI)_2$ in acetonitrile and a reference polyaniline (PANI) film (Figure 6). The spectrum of the reference PANI film (blue trace, Figure 6) exhibits characteristic features of the emeraldine salt form, including π–π^* transitions of benzenoid rings and quinoid ring structures at 325 nm and 380 nm, and a broad absorption band spanning 450–700 nm, associated with polaronic transitions and delocalized charge carriers in the doped polymer matrix [41, 42]. These features serve as benchmarks for identifying polyaniline-like structures.

In comparison, the poly(PW_{11}-ANI) film displays a similar spectral profile (red trace, Figure 6), supporting the successful

23669608, 2026, 15, Downloaded from https://onlinelibrary.wiley.com/doi/10.1002/smtd.70834 by Spanish Cochrane National Provision (Ministerio de Sanidad), Wiley Online Library on [04/11/2026]. See the Terms and Conditions (https://onlinelibrary.wiley.com/terms-and-conditions) on Wiley Online Library for rules of use; OA articles are governed by the applicable Creative Commons License

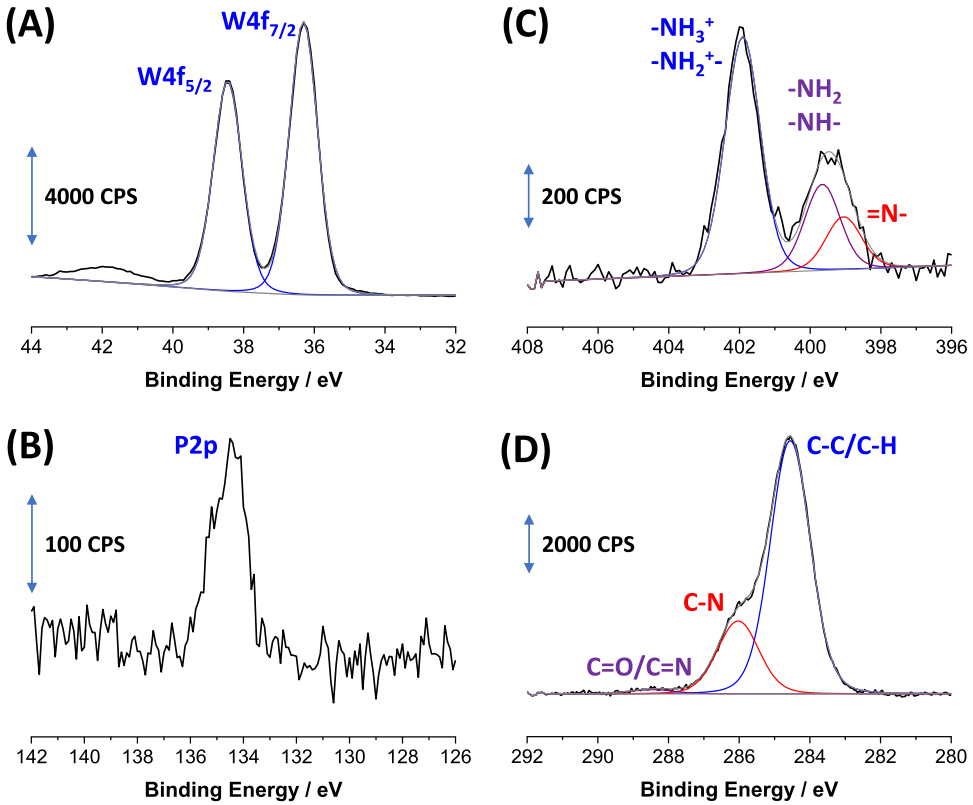


FIGURE 7 | High-resolution XPS spectra of poly(PW_{11}-ANI) generated by electropolymerization on ITO: (A) W 4f spectrum showing characteristic doublet peaks ($W4f_{7/2}$ and $W4f_{5/2}$); (B) P 2p region indicating the incorporation of phosphorus from the Keggin-type polyoxometalate structure; (C) N 1s spectrum deconvoluted into three components (protonated amine, $-NH_3^+$ & $-NH_2^+-$, primary and secondary amine, $-NH_2$ & $-NH-$, and imine, $=N-$), consistent with polyaniline-like structures depicted in scheme 2; (D) C 1s spectrum showing components assigned to C—C/C—H, C—N, and C═O/C═N bonds, indicative of the polymeric matrix and residual oxygen-containing species.

formation of a polyaniline-type backbone. However, notable shifts in peak position and intensity are observed, underscoring the influence of PW_{11} functionalization. A strong absorption band centered near 390 nm, assigned to quinoid ring transitions, is red-shifted and more intense than that of the reference PANI, suggesting an altered electronic environment induced by the POM units. Additionally, the broad band between 500 nm and 700 nm is more pronounced in the hybrid film, indicating enhanced polaron formation and/or facilitated charge transfer processes promoted by the inorganic framework [43]. These features are absent from the **PW_{11}-(ANI)$_2$** monomer spectrum (black trace, Figure 6), confirming the formation of the PANI junctions. The monomeric POM units are known absorbing light at 265 nm, but one cannot investigate the wavelength region below 300 nm for the poly(PW_{11}-ANI) film on ITO due to overlap with ITO absorption band [44].

These spectral differences indicate that while the hybrid retains the essential optical fingerprints of polyaniline, the incorporation of POM clusters substantially modifies its electronic structure. The observed red shifts and increased absorption intensities likely arise from electronic delocalization and coordination interactions between the aniline units and the tungsten-based polyoxometalate. Collectively, these findings highlight the successful electropolymerization of the hybrid monomer and the formation of a functionalized polymer film with distinct and potentially enhanced optoelectronic properties relative to conventional PANI.

2.1.6.2 | Chemical Surface Analysis. X-ray photoelectron spectroscopy (XPS) was used to characterize the surface composition and chemical states of poly(PW_{11}-ANI) films electropolymerized on ITO. The survey spectrum revealed W, P, and O from the polyoxometalate and C, N from the polyaniline moieties, along with the expected In and Sn signals from the ITO substrate. The detection of W and P is associated with the successful immobilization of the POM units, while C and N signals verified the presence of the aniline-derived polymer matrix.

High-resolution spectra provided insights into the chemical environments of the key elements to emphasize structural specificities of poly(PW_{11}-ANI) (Figure 7A–D). The W 4f core-level spectrum (Figure 7A) is dominated by the W^{6+} spin–orbit doublet, with the W $4f_{7/2}$ and W $4f_{5/2}$ components centered at 36.1 and 38.2 eV, respectively, yielding a spin–orbit splitting of 2.1 eV, consistent with a Keggin-type PW_{11} structure. The P 2p spectrum (Figure 7B) exhibits a single peak at 134.2 eV, assigned to P^{5+} within the phosphate unit, confirming preservation of the polyoxometalate structural integrity. The C 1s and N 1s core-level spectra (Figure 7C,D) exhibit features characteristic of polyaniline. The C 1s spectrum can be deconvoluted into components centered at 284.6 eV and 285.6 eV, assigned to C—C/C—H and C—N

23669608, 2026, 15, Downloaded from https://onlinelibrary.wiley.com/doi/10.1002/smtd.70834 by Spanish Cochrane National Provision (Ministerio de Sanidad), Wiley Online Library on [04/11/2026]. See the Terms and Conditions (https://onlinelibrary.wiley.com/terms-and-conditions) on Wiley Online Library for rules of use; OA articles are governed by the applicable Creative Commons License

environments, respectively, together with a minor contribution at higher binding energy (288.5 eV) attributed to some trace of oxidized carbon (C═O) species. The N 1s spectrum is resolved into three components located at 398.7, 399.9, and 401.7 eV, corresponding to quinoid imine, benzenoid amine, and protonated nitrogen species, respectively. This is consistent with the formation of quinoid nitrogen sites upon electropolymerization [45]. Collectively, these results confirm that the hybrid films preserve the polyoxometalate framework while incorporating electroactive polyaniline, a structure essential for their anticipated electrochemical accessibility and electrocatalytic performance.

2.2 | Poly(PW_{11}-ANI) Nanofilaments in Mesoporous Silica Films

2.2.1 | Electrochemical Behavior and Evidence of the Electropolymerization Process of PW_{11}-$(ANI)_2$ Within Vertically Oriented Mesoporous Silica Films (VMSFs) on ITO

In view of getting poly(PW_{11}-ANI) in the form of individual nanofilaments, which could improve the electrochemical properties of the polymer owing to nanoscale confinement (as pointed out for PANI [37, 46]), we have explored the electrochemical polymerization of PW_{11}-$(ANI)_2$ by multi-sweep CV within VMSFs made of nanochannels of various diameters (2.0, 3.0 and 4.3 nm) orthogonal to the ITO surface (Figure 8). No noticeable voltammetric signals and no electropolymerization were observed through the VMSF with narrower pore size (see Figure 8A), most likely due to impeded diffusion of the PW_{11}-$(ANI)_2$ units and/or ineffective chain propagation in so small nanochannels (2.0 nm). By contrast, ITO electrodes covered with VMSFs with larger pore diameters (3.0 and 4.3 nm) enabled effective electropolymerization (as evidenced by multi-sweep CV, see parts B & C of Figure 8), albeit with cathodic peak currents slightly lower than those obtained on bare ITO under identical conditions (compare to Figure 1B) due to mass transport limitation imposed by the mesoporous silica film, demonstrating that a critical pore size is required to allow the monomer to pass through VMSF and reach the electrode surface and promote the growth of the polymer chains inside the mesopores. The intensity of the first voltammetric signals (for both the cathodic wave of the POM and the NH_2 oxidation peak) was approximately twice as large when going from VMSF with a pore diameter of 3.0 nm to that of 4.3 nm, underscoring a less marked diffusional constraint in the latter case. For the same reason, the polymer growth rate (identifiable by the increase in currents over successive potential cycles) was faster in 4.3 nm nanochannels, with however lower steady-state peak currents values after 100 cycles (compare red curves in parts B & C of Figure 8), which can be related to the lower surface density of pores compare to that of 3.0 nm nanochannels. These findings highlight the pivotal role of pore size in governing both transport phenomena and polymerization kinetics under confinement. The next experiments will mainly be carried out with poly(PW_{11}-ANI) in VMSF with a pore diameter of 3.0 nm. It should be noted that it is also possible to apply an electrografting step of the underlying ITO surface prior to electropolymerization through the VMSF, both processes being as effective as for bare ITO (see Figures S8 and S9).

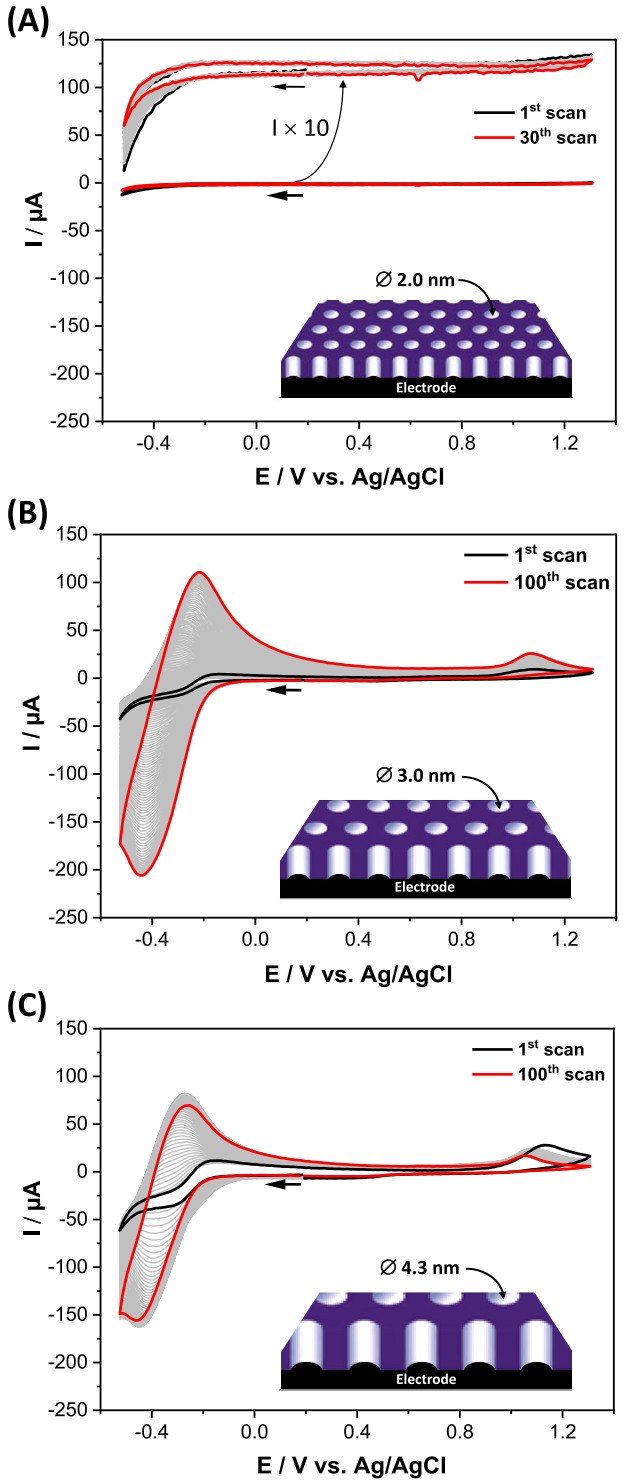


FIGURE 8 | Comparison of the electropolymerization CV profiles (recorded at a scan rate of 100 $mV.s^{-1}$) in a solution containing 2.5 mM PW_{11}-$(ANI)_2$ in acetonitrile/aqueous 0.2 M $HClO_4$ (1/1 vol/vol) within VMSFs of (A) 2.0 nm, (B) 3.0 nm, and (C) 4.3 nm pore sizes.

2.3 | Analysis of the Growth Profile of Poly(PW_{11}-ANI) Within VMSFs

Figure 9A compares the growth profile of poly(PW_{11}-ANI) electropolymerized within vertically aligned mesoporous silica thin films featuring 3 nm pore channels to that obtained on bare

23669608, 2026, 15, Downloaded from https://onlinelibrary.wiley.com/doi/10.1002/smtd.70834 by Spanish Cochrane National Provision (Ministerio de Sanidad), Wiley Online Library on [04/11/2026]. See the Terms and Conditions (https://onlinelibrary.wiley.com/terms-and-conditions) on Wiley Online Library for rules of use; OA articles are governed by the applicable Creative Commons License

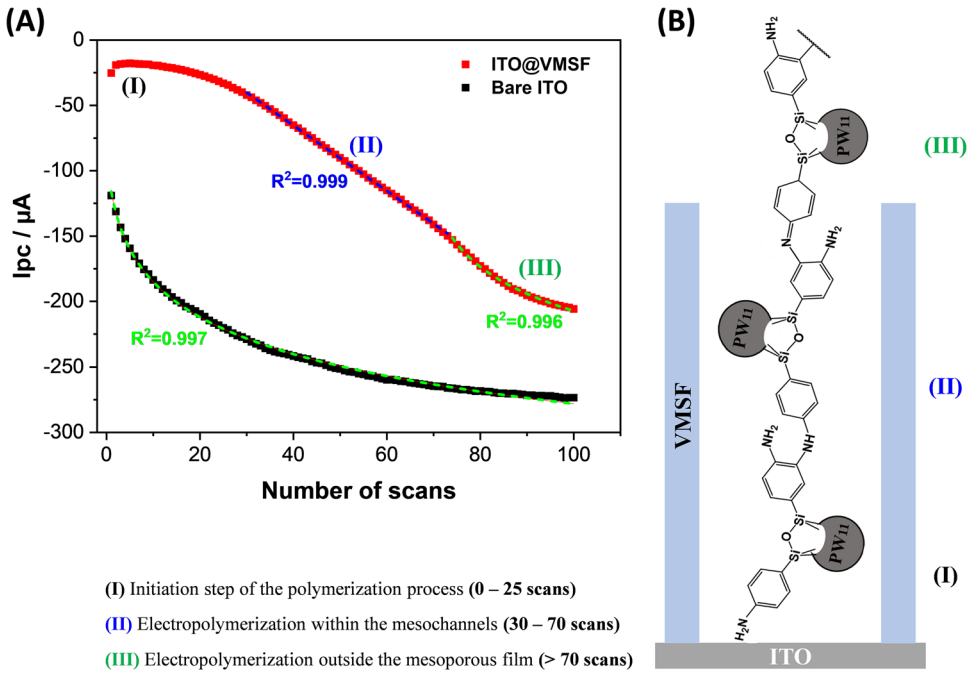


FIGURE 9 | (A) Growth profile of poly(PW_{11}-ANI) derived from the cathodic peak currents (I_{pc}) during successive CV scans, obtained by direct electropolymerization of PW_{11}-$(ANI)_2$ in acetonitrile / aqueous 0.2 M $HClO_4$ (1/1 vol/vol) on bare ITO (black squares) and within VMSF on ITO (red squares), along with the fitting curves corresponding to region II (blue) and Region 3 (green). (B) Schematic representation of the three growth stages of the organic–inorganic hybrid poly(PW_{11}-ANI) through the a mesopore channel (PW_{11} units and chain length not at scale).

ITO electrode under identical conditions, by plotting the cathodic peak currents associated with the reduction of tungsten centers (monitored at (-0.42 V vs. Ag/AgCl) during successive CV scans. The distinct kinetic behaviors underscore the influence of the nanoconfined environment on the polymerization process. In the mesostructured films, the current evolution followed a three-stage growth pattern (see red curve on Figure 9A). The initial phase (Region I, scans 1–25) exhibited a slow and gradual increase in cathodic current, corresponding to the nucleation and initiation of polymer growth within the mesopores. This was followed by a second phase (Region II, scans 30–70), characterized by a rapid rise in peak current, indicative of accelerated polymer chain propagation within the accessible pore volume. Beyond 70 scans, a third region (Region III, scans 70–100) displayed a slower but continuous current increase, which is attributed to the extension of the polymer beyond the mesoporous framework, likely involving growth on the outer surface of the silica film (as illustrated in Figure 9B). The same growth profile analysis was performed by also following the cathodic current evolution with vertically-oriented silica films of 4.3 nm pore size (see Figure S10). It is worth mentioning that the nucleation/initiation phase in this case is almost imperceptible, and a significant increase of the cathodic current is immediately observed after the first scan which seem to indicate that the transport phenomena involved in the electropolymerization process are faster. The three-stage kinetic profile observed for the VMSF contrasts sharply with the more uniform growth observed on bare ITO (Figure 1B) and also illustrated by the black curve in Figure 9A, highlighting the critical role of spatial confinement in directing the electropolymerization mechanism and the resulting nanostructure of the hybrid material.

2.4 | Electrochemical Characterization of Poly(PW_{11}-ANI) Nanofilaments in VMSF

The electrochemical behavior of poly(PW_{11}-ANI) nanofilaments electropolymerized within mesoporous silica matrices with a pore size of 3.0 nm (as in Figure 8B) was investigated in acetonitrile containing 0.1 M *n*-$BuNClO_4$, using ITO substrates either as is (see left part of Figure 10) or modified with a pre-electrografted monolayer of PW_{11}-$(ANI)_2$ (see right part of Figure 10). CV curves were recorded at a scan rate of 50 $mV.s^{-1}$ over a potential window starting in the cathodic direction down to -0.55 V, followed by an anodic sweep up to +1.30 V versus Ag/AgCl (see parts A & B in Figure 10) or at various scan rates in the narrow potential window corresponding to the POM signal (see parts C & D in Figure 10). The electrochemical response of poly(PW_{11}-ANI) confined within the nanoporous matrix resembles that observed on bare ITO, suggesting few or no effect of the silica matrix on the electrochemistry of the confined POM, which is a good point considering that medium effects can occur in the voltammetry of POMs [47]. As shown in Figure 10A,B, a reversible CV signal centered at -0.41 V versus Ag/AgCl appeared during the first cathodic scan, attributed to the reduction of tungsten centers. During the subsequent anodic sweep up to +1.30 V, an additional broad irreversible oxidation wave emerged at approximately +0.95 V, along with some contribution of PANI junction around +0.40 V. Notably, a new irreversible reduction peak developed in the second scan at -0.25 V, consistent with the behavior previously reported on bare ITO (Figure 5B). Although the overall shape of CV curves remained unchanged for the polymer obtained after ITO electrografting, the electrochemical response of the poly(PW_{11}-ANI) was significantly enhanced (peak

23669608, 2026, 15, Downloaded from https://onlinelibrary.wiley.com/doi/10.1002/smtd.70834 by Spanish Cochrane National Provision (Ministerio de Sanidad), Wiley Online Library on [04/11/2026]. See the Terms and Conditions (https://onlinelibrary.wiley.com/terms-and-conditions) on Wiley Online Library for rules of use; OA articles are governed by the applicable Creative Commons License

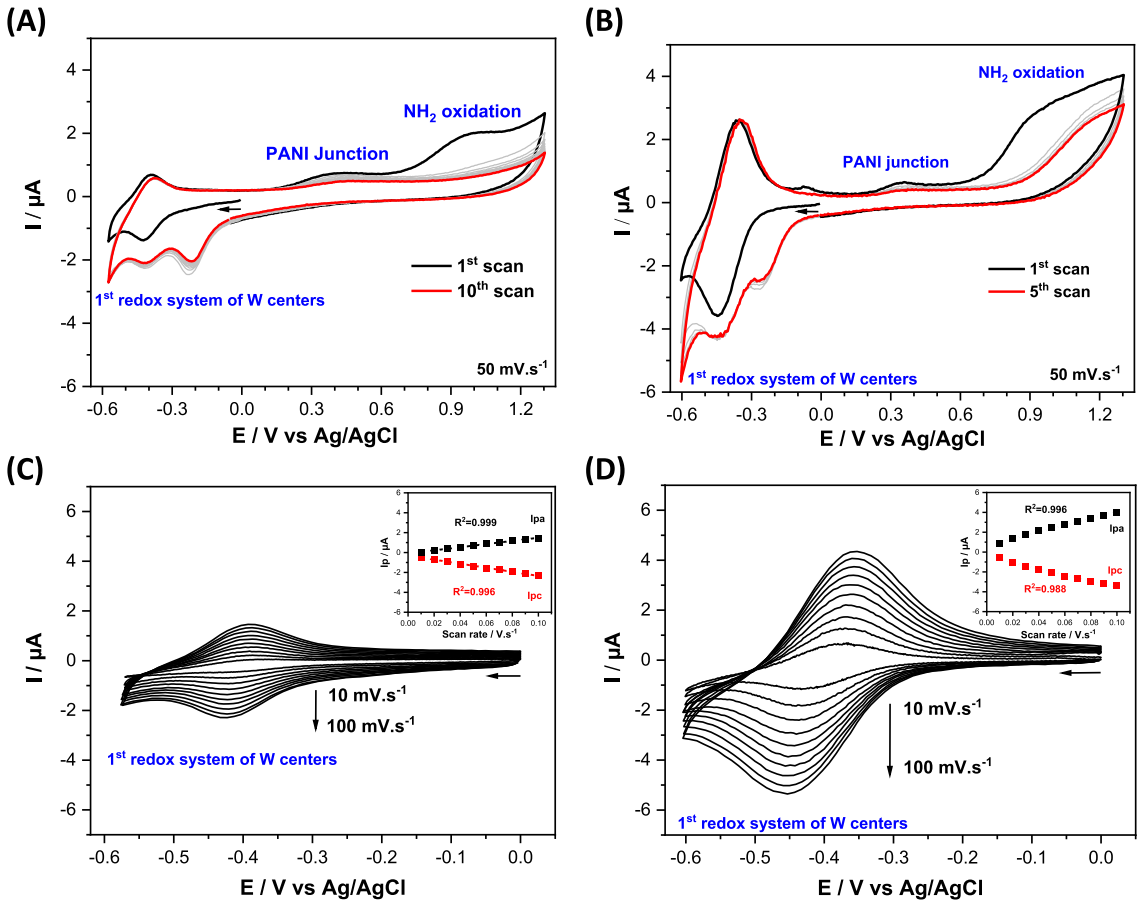


FIGURE 10 | (A,B) Cyclic voltammetry characterization of poly(PW_{11}-ANI) nanofilaments electropolymerized within VMSF with 3.0 nm pore size as in Figure 8B, respectively without (A) and with (B) prior electrografting with PW_{11}-(ANI)(diaz), as recorded at 50 $mV.s^{-1}$ in ACN + 0.1 M *n*-Bu_4NClO_4 in a broad potential window showing the redox processes of both W centers and electropolymerized aniline moieties. (C,D) CV curves recorded at various potential scan rates (from 10 to 100 $mV.s^{-1}$) in a narrower potential window corresponding to the first redox system of W centers, in acetonitrile / aqueous 0.2 M $HClO_4$ (1/1 vol/vol) for the same samples as in (A), (B), with variations of peak currents as a function of scan rate in inserts.

currents twice as large, compare parts A & B in Figure 10). This suggests faster growth of the nanofilaments when the monomer is already present at the bottom of the silica pores and/or a better stabilization (more effective immobilization) of poly(PW_{11}-ANI) in VMSF. This was also confirmed by focusing on the narrow potential window corresponding to the POM signal (with more intense signals observed after electrografting, compare parts C & D in Figure 10), and the linear variation of peak currents with potential scan rates indicate a thin-layer behavior. Surface concentrations of POM of 4.2×10^{-11} $mol.cm^{-2}$ and 1.6×10^{-10} $mol.cm^{-2}$ were measured for poly(PW_{11}-ANI) nanofilaments respectively electropolymerized without and with prior electrografting. These values are, as expected, lower than those obtained for the bulky poly(PW_{11}-ANI) films generated on bare ITO (see section 3.1.5) due to the restricted accessible electrode surface area imposed by the presence of VMSF. Similar results were observed for poly(PW_{11}-ANI) nanofilaments electropolymerized within mesoporous silica matrices with a pore size of 4.3 nm (see Figure S11), leading to a surface concentration of POM of 1.8×10^{-10} $mol.cm^{-2}$ for poly(PW_{11}-ANI) electropolymerized without electrografting, indicating than more electroactive polymer can be accommodated into the channels of larger pore.

2.5 | Morphological and Structural Characterization of Poly(PW_{11}-ANI) Nanofilaments in VMSF

XPS was first employed to investigate the surface composition and chemical states of poly(PW_{11}-ANI) films electropolymerized within VMSF on ITO substrates. The survey spectrum confirmed the presence of W, P, and O from the polyoxometalate units, as well as C and N from the polyaniline moieties, The detection of W and P provided clear evidence of successful incorporation of the POM units within the hybrid matrix, while the presence of C and N verified the formation of the aniline-derived polymer backbone. As illustrated in Figure 11, high-resolution spectra offered deeper insights into the local chemical environments. The W 4f region, centered at 36.1 eV (Figure 11A), displayed the characteristic spin–orbit doublet of W^{6+}, in good agreement with the Keggin-type PW_{11} structure, together with minor contributions from partially reduced W^{5+} species. The minor contribution of W(V) species is therefore attributed to partial reduction occurring during electrochemical cycling and/or to electronic interactions with the conducting polymer matrix, rather than to the electropolymerization process itself. The P 2p spectrum exhibited a peak at 134.2 eV (Figure 11B), attributable

23669608, 2026, 15, Downloaded from https://onlinelibrary.wiley.com/doi/10.1002/smtd.70834 by Spanish Cochrane National Provision (Ministerio de Sanidad), Wiley Online Library on [04/11/2026]. See the Terms and Conditions (https://onlinelibrary.wiley.com/terms-and-conditions) on Wiley Online Library for rules of use; OA articles are governed by the applicable Creative Commons License

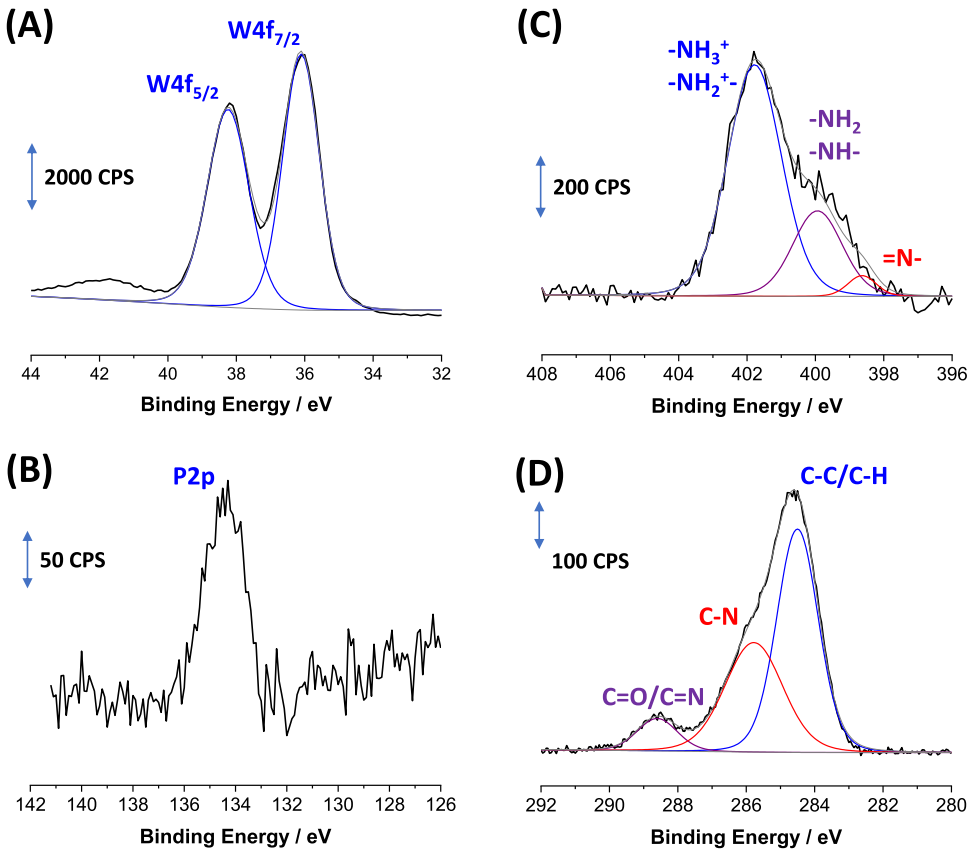


FIGURE 11 | High-resolution XPS spectra of poly(PW_{11}-ANI) nanofilaments electropolymerized $PW_{11}(ANI)_2$ within VMSF with 3.0 nm pore size (as in Figure 8B): (A) W 4f spectrum showing characteristic doublet peaks ($W4f_{7/2}$ and $W4f_{5/2}$); (B) P 2p region, (C) N 1s spectrum deconvoluted into three components corresponding to protonated and non-protonated amine and imine moieties; (D) C 1s spectrum showing components assigned to C—C/C—H, C—N, and C═O/C═N bonds, indicative of the polymeric matrix and residual oxygen-containing species.

to P^{5+} in a phosphate environment, confirming the preservation of the POM framework within the mesoporous scaffold. The C 1s (Figure 11C) and N 1s (Figure 11D) regions revealed spectral features typical of polyaniline. In the C 1s spectrum (Figure 11C), peaks at 284.8, 286.6, and 288.7 eV correspond to C—C/C—H, C—N, and C═O/C═N species. Three different types of nitrogen species can be identified in the N 1s spectrum, with peaks located at 398.7, 399.9, and 401.8 eV, such as benzenoid amines, quinoid imines, and protonated amines, consistent with a partially doped emeraldine state [48]. The relative peak broadening observed here for poly(PW_{11}-ANI) nanofilaments compared to bulky deposits on bare ITO (Figure 7) is probably due to electrostatic interactions with the mesoporous silica surface [49]. The relative contributions of the different nitrogen species indicate partial protonation of the polymer backbone, supporting the presence of a doped polyaniline state and suggesting charge delocalization within the hybrid framework. In addition, a slight shift and broadening of the W 4f signals compared to the pristine POM are observed, pointing to a modified electronic environment consistent with electronic coupling and possible charge transfer between the polyoxometalate units and the polymer matrix. In summary, these results confirm that the hybrid poly(PW_{11}-ANI) films retain the structural integrity of the polyoxometalate while integrating it within an electroactive polyaniline network confined in mesoporous silica. This architecture is essential for the fabrication of nanometric hybrid structures exhibiting promising electrocatalytic functionality.

Further characterization was made by transmission electron microscopy (TEM), energy dispersive x-ray spectroscopy (EDS) and grazing-incidence small-angle x-ray scattering (GISAXS), as illustrated in Figure 12. After electropolymerization of PW_{11}-$(ANI)_2$ through VMSF, the overall morphology and structural orientation of the mesoporous silica matrix remained unchanged, as pointed out by TEM analysis revealing from a cross-section view a membrane of uniform thickness (110 nm) made of parallel and orthogonally oriented nanochannels with a pore-to-pore separation of about 4 nm (Figure 12A). This indicates that the polymerization process does not affect the structural integrity of the silica framework. This was also supported by GISAXS data (Figure 12B), confirming a high level of mesostructural order over the wide area of VMSF on ITO on the basis of well-defined diffraction spots in the equatorial plane (scattering of the (10), (11) and (20) planes of the vertical and hexagonal mesostructure). The scattering maxima values of the main signal ((10) plane) before and after electropolymerization are equal (q_{max} = 1.57 nm^{-1}), corresponding to a *d*-spacing of 4.0 nm, consistent with the value reported for VMSF prepared by EASA using the same ODAB surfactant (1.55 nm^{-1}) [46]. This stability suggests that the electrochemical conditions employed for the growth of poly(PW_{11}-ANI) nanofilaments are compatible with keeping intact the mesoporous architecture, preserving its uniform porosity and orientation while allowing successful incorporation of the functional hybrid material. Moreover, EDS measurements performed at various places of the mesochannels

23669608, 2026, 15, Downloaded from https://onlinelibrary.wiley.com/doi/10.1002/smtd.70834 by Spanish Cochrane National Provision (Ministerio de Sanidad), Wiley Online Library on [04/11/2026]. See the Terms and Conditions (https://onlinelibrary.wiley.com/terms-and-conditions) on Wiley Online Library for rules of use; OA articles are governed by the applicable Creative Commons License

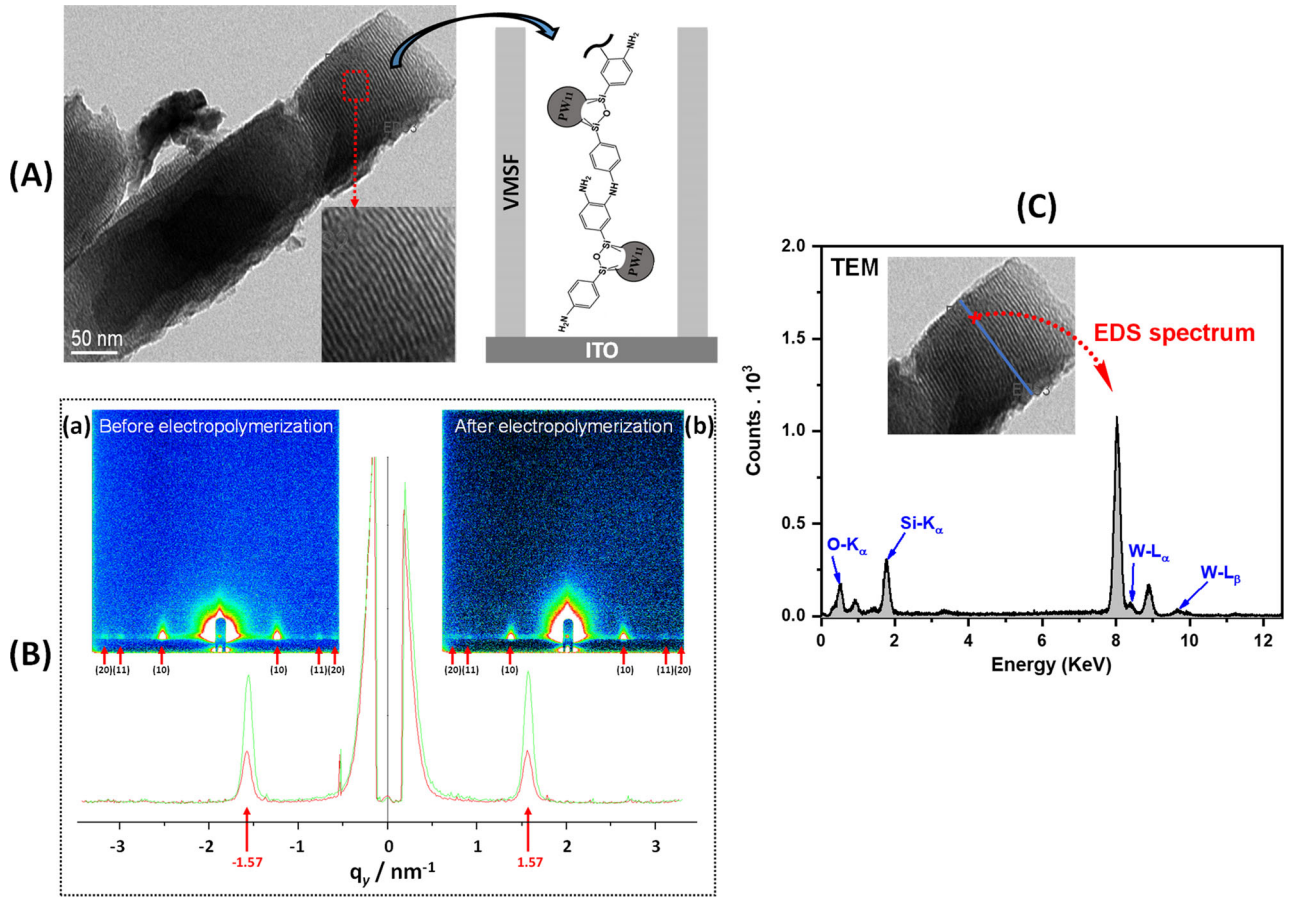


FIGURE 12 | (A) TEM micrograph (cross sectional view) of mesoporous silica film with 3.0 nm pore size after electropolymerization of PW_{11}-$(ANI)_2$ (as in Figure 8B) with higher magnification in insert. (B) 2D and 1D GISAXS patterns of the VMSF before (part (a), green curve) and after (part (b), red curve) electropolymerization of PW_{11}-$(ANI)_2$ (red arrows indicate the position of diffraction spots in the equatorial plane). (C) EDS spectrum recorded at the position marked with a red cross on the TEM cross section corresponding to the analysis of poly(PW_{11}-ANI) nanofilaments in the mesoporous silica membrane.

(see one example in Figure 12C) reveal the presence of the characteristic rays of polyoxometalate structures (W-Lα, W-Lβ, and O-Kα), thus confirming the presence of POM inside the VMSF.

It should be noted that direct morphological visualization of individual polymer strands within the VMSF nanochannels remains challenging due to the limited spatial resolution and contrast of conventional electron microscopy for such confined hybrid systems. While cross-sectional TEM confirms the presence of an ordered mesoporous structure and EDS mapping evidences the incorporation of tungsten-containing species within the channels, these techniques do not allow direct observation of discrete filamentary objects.

Nevertheless, the progressive increase of the electrochemical response during electropolymerization, together with the retention of redox activity after rinsing, provides strong indirect evidence for the formation of surface-confined, extended species within the nanochannels. At the same time, it cannot be unambiguously determined whether these species correspond to long polymer chains or shorter oligomeric segments. Therefore, the term "nanofilaments" is used here in a descriptive sense to refer to confined polymeric growth within one-dimensional channels, rather than implying direct morphological visualization of discrete filamentary objects.

2.6 | Electrocatalytic Activity of Poly(PW_{11}-ANI) Toward the Reduction of Nitrites

To illustrate the potential interest of the oriented nanocomposite films made of poly(PW_{11}-ANI) nanofilaments in mesoporous silica, a preliminary investigation of their electrocatalytic response to nitrite reduction was carried out and compared to that of poly(PW_{11}-ANI) synthesized on bare ITO, as illustrated in Figure 13.

As this reaction is expected to happen in aqueous medium, we first investigated the electrochemical behavior of the polymer by CV in aqueous solution (+0.2 M $HClO_4$). Three redox waves can be distinguished (respectively around -0.45, -0.55, and -0.65 V vs. Ag/AgCl), corresponding to the three successive reduction steps of the POM (Figure 13A). Their intensity was in the same order as peak current values measured in acetonitrile (i.e., surface concentration of POM following the same trend: poly(PW_{11}-ANI) nanofilament < poly(PW_{11}-ANI) on bare ITO < poly(PW_{11}-ANI) on electrografted ITO), confirming that the immobilized

23669608, 2026, 15, Downloaded from https://onlinelibrary.wiley.com/doi/10.1002/smtd.70834 by Spanish Cochrane National Provision (Ministerio de Sanidad), Wiley Online Library on [04/11/2026]. See the Terms and Conditions (https://onlinelibrary.wiley.com/terms-and-conditions) on Wiley Online Library for rules of use; OA articles are governed by the applicable Creative Commons License

POM units remained electrochemically accessible in aqueous medium.

In the presence of nitrite, all poly(PW_{11}-ANI) modified electrodes gave rise to well-defined electrocatalytic responses with an onset potential of around -0.1 V versus Ag/AgCl, yet with some differences (Figure 13B). In spite of the lowest peak currents recorded with poly(PW_{11}-ANI) nanofilaments in VMSF, this hybrid polymer in the mesochannels was characterized by the most significant increase of the cathodic currents recorded in presence of nitrite and more effective electrocatalysis compared to the response with poly(PW_{11}-ANI) on bare ITO electrode. This unexpected result highlights the interest of poly(PW_{11}-ANI) nanostructuration in a linear configuration as greater electrocatalytic activity is usually observed when more POM units are loaded on the electrode surface [50]. In the absence of POM, no noticeable cathodic wave was observed (only a small current increase at potentials below -0.6 V), consistent with the electrocatalytic properties of Keggin derivatives toward nitrite electroreduction [51]. Interestingly, the high catalytic current observed for poly(PW_{11}-ANI) within VMSF was characterized by a sharp increase, in the form of a wave better defined than similar POMs immobilized with an ionic liquid [52]. It suggests that the linear configuration of poly(PW_{11}-ANI) in the silica nanochannels can lead to improved electrocatalytic activity compared to that recorded for bulky metallopolymers on bare electrode, which likely have a more compact arrangement of POM units. Tafel analysis performed in the kinetically controlled region of the LSV curves yielded slopes of 199 $mV{\cdot}dec^{-1}$ for poly(PW_{11}-ANI) on bare ITO, regardless of whether a prior electrografting step was applied, and 172 $mV{\cdot}dec^{-1}$ for poly(PW_{11}-ANI) nanofilaments confined within VMSF (Figure 13C). Both values exceed the theoretical 120 $mV{\cdot}dec^{-1}$ expected for a single rate-determining electron transfer step, suggesting that the electrocatalytic process involves a complex multi-step mechanism in which adsorption of the nitrite substrate and/or internal charge transport within the polymer film contributes to the overall kinetics [53, 54] The identical Tafel slopes obtained for films prepared with and without electrografting confirm that the covalent anchoring of the polymer to the ITO surface does not alter the intrinsic kinetics of the nitrite reduction reaction. By contrast, the lower Tafel slope observed for the nanofilaments in VMSF (Figure 13C) indicates a significant modification of the reaction pathway induced by nanoscale confinement in the mesochannels, suggesting improved accessibility and local environment of the POM active sites in the oriented linear configuration. The stability of poly(PW_{11}-ANI) during the electrocatalytic measurements was evaluated by chronoamperometry for 3600 s at –0.57 V vs Ag/AgCl in the presence of 1 mM NO_2^- on bare ITO and into the VMSF (Figure 13D). For ITO@Poly(PW_{11}-ANI), the catalytic current is relatively stable over time, confirming efficient catalytic turnover and good operational stability. This conclusion is further supported by the nearly superimposable CV curves recorded over 3600 s (see Figure S12). For ITO@VMSF_Poly(PW_{11}-ANI), the catalytic current also remained relatively stable during the first 1500 s and is higher than that observed for ITO@Poly(PW_{11}-ANI), consistent with the enhanced electrocatalytic response evidenced by LSV measurements (Figure 13B). Beyond this period, a slight increase in the catalytic current is observed. This behavior may be attributed to the gradual accumulation of NO_2^- ions within the mesochannels of the VMSF, promoted by the positive surface charge of the silica walls at the working pH. Nevertheless, additional investigations are required to elucidate the mechanism responsible for this behavior and to fully understand the origin of the observed current increase.

Anyway, the preliminary results obtained in this section confirm that the arrangement imposed by the linear, robust, and stable configuration of the vertically-oriented mesoporous silica thin films used to confine electroactive polyoxometalates confers a significant advantage for electrocatalytic purposes.

2.7 | Comparative Overview of Recent POM-Polymer Hybrid Systems

Table 1 presents a comparative overview of representative POM-polymer hybrid systems recently reported in the literature. The comparison focuses on synthesis methods, POM incorporation modes, characterization approaches, and applications, thereby highlighting the unique one-step fabrication strategy and structural features of the poly(PW_{11}-ANI) hybrid polymer developed in this work.

To the best of our knowledge, no previous study on POM-polymer systems has reported an electropolymerization mechanism initiated by the electrochemical reduction/oxidation of the POM core, followed by the coupling of the resulting radical cations. This finding highlights the novelty of the proposed approach, both in terms of the polymerization mechanism and the confinement of the resulting hybrid polymer within vertically oriented mesoporous silica, thereby offering new opportunities for the development of nanostructured POM-based materials with enhanced properties and functionalities.

3 | Conclusion

In summary, we report the first example of an organic–inorganic hybrid polymer incorporating covalently bound polyoxometalate units, PW_{11}, directly into the polymer backbone, obtained via electropolymerization of a single monomer bearing two electropolymerizable aniline groups, PW_{11}-$(ANI)_2$, onto an ITO electrode. This molecular design enables the direct integration of redox-active POM clusters within the conjugated polymer network, providing a robust and versatile route for constructing hybrid materials with tailored electrochemical functionality. Furthermore, a preliminary electrografting step significantly enhances the electrodeposition process and the amount of POM units deposited onto the ITO surface in the resulting polymer film, likely due to improved interfacial adhesion and polymer growth control. Importantly, this electropolymerization strategy was also successfully applied within vertically oriented mesoporous silica films, enabling the formation of individual poly(PW_{11}-ANI) nanofilaments confined within a nanostructured environment, leading to improved electrocatalytic properties compared to bulky films. These findings open new avenues for the bottom–up fabrication of functional hybrid nanomaterials with potential applications in electrochemical devices, sensing, or energy storage. These results highlight that nanoscale confinement of the POM units within the electropolymerized matrix not only ensures high loading and prevents leaching but also enhances catalytic

23669608, 2026, 15, Downloaded from https://onlinelibrary.wiley.com/doi/10.1002/smtd.70834 by Spanish Cochrane National Provision (Ministerio de Sanidad), Wiley Online Library on [04/11/2026]. See the Terms and Conditions (https://onlinelibrary.wiley.com/terms-and-conditions) on Wiley Online Library for rules of use; OA articles are governed by the applicable Creative Commons License

TABLE 1 | POM-polymer hybrid systems: synthesis, structure, and applications.

POM-polymer material	Synthesis procedure	POM characterization	POM arrangement within the hybrid material	Application/efficiency	Refs.
PW_{12}-doped polypyrrole hybrid film	Electrodeposition at 1.1 V versus Ag/AgCl of 0.1 M pyrrole and 5 mM phosphotungstic acid (PW_{12}) in CH_3CN on FTO (30–120 s)	PW_{12} confirmed by SEM-EDX, IR, and XRD	PW_{12} acts as a dopant anion in the PPy matrix (noncovalent entrapment)	**Dye-sensitized solar cells** / Average power conversion efficiency: 6.19% under 100 $mW{\cdot}cm^{-2}$.	[55]
Keggin POM-based 3D coordination polymer materials	Hydrothermal synthesis by mixing POM precursor ($HPMo_9W_3O_{40}$ (1), $HPW_9Mo_3O_{40}$ (2), $H2SiMo_9Mo_3O_{40}$ (3)), $CuCl_2$ and 4-atrz ligand	POM presence confirmed by CV, IR, and XRD	POM anions trapped between ring-like Cu^1-4-atrz complexes as connecting nodes in a 3D sandwich-like network	**Supercapacitors and NO_2^- sensing** / Specific capacitances: 231.7 (1), 147.5 (2), 232.5 $F{\cdot}g^{-1}$ (3) at 1 $A{\cdot}g^{-1}$; NO_2^- sensitivity: 0.242 $\mu A{\cdot}\mu M^{-1}$; LOD: 4.2 μM (linear range $6{\times}10^{-6}$–$1.0{\times}10^{-4}$ M).	[56]
Covalently linked POM–polypyrrole hybrids	Co-electropolymerization of pyrrole with POM-functionalized pyrrole monomer (aryl-imido linkage) by CV (−0.2 to +1.8 V) in dry CH_3CN / 0.1 M Bu_4NBF_4 on GC, FTO and Pt	POM core confirmed by XPS, IR, and CV	First reported covalent POM–PPy hybrid via electropolymerization of a POM-derivatized monomer; POM grafted to PPy chain	**Capacitive energy storage** / Specific capacitance enhanced; 95% capacitance retention over 1200 cycles; decreased charge-transfer resistance.	[57]
GO-PPy / $SiMo_2VW_9$ nanohybrid	In situ oxidative polymerization of pyrrole in the presence of graphene oxide and $SiMo_2VW_9$ for 24 h at room temperature	POM confirmed by CV, FTIR, XRD, FE-SEM, EDX, and XPS	POM units and PPy distributed across GO sheets; POM acts as a dopant anion in the PPy–GO matrix	**Capacitive energy storage** / Specific capacitance: 351.6 $F{\cdot}g^{-1}$ at 0.5 $A{\cdot}g^{-1}$; energy density: 999.93 $W{\cdot}kg^{-1}$; 80% capacitance retention after 5000 cycles at 8 $A{\cdot}g^{-1}$.	[58]

(Continues)

23669608, 2026, 15, Downloaded from https://onlinelibrary.wiley.com/doi/10.1002/smtd.70834 by Spanish Cochrane National Provision (Ministerio de Sanidad), Wiley Online Library on [04/11/2026]. See the Terms and Conditions (https://onlinelibrary.wiley.com/terms-and-conditions) on Wiley Online Library for rules of use; OA articles are governed by the applicable Creative Commons License

TABLE 1 | (Continued)

POM-polymer material	Synthesis procedure	POM characterization	POM arrangement within the hybrid material	Application/efficiency	Refs.
$\{Ni_{14}SiW_9ale_7\}$-doped PEDOT hybrid film	Chronocoulometry at +0.85 V versus Ag/AgCl to electrodeposit $Ni_{14}SiW_9Ale_7$ POM within PEDOT matrix	POM units characterized by CV	Electrostatic interactions between high-charge POM anions and PEDOT matrix favor doping; non-covalent entrapment	No electrochemical application reported.	[59]
PEDOT/NiPOM composite film	Electropolymerization of EDOT in the presence of $K_7[Ni^3Ni^2(H_2O)W_{11}O_{39}]\cdot 15H_2O$ in $LiClO_4$ solution	POM presence confirmed by CV, FTIR, XPS, and SEM–EDX	POM acts as dopant anion within the PEDOT matrix (noncovalent entrapment)	**Glucose sensing** / Sensitivity: 272 $\mu A\cdot\mu M^{-1}.cm^{-2}$; LOD: 1.09 μM, linear range: 0.1 – 10 mM).	[60]
Covalent Silyl polyoxophosphotungstate–porphyrin copolymers	The polymers poly-$PW_{11}Si_2$-ZnOEP, poly-$PW_{11}Si_2$-H_2T_2P, poly-$P_2W_{17}Si_2$-ZnOEP, poly-$P_2W_{17}Si_2$-H_2T_2P are synthesized by a chemical copolymerization initiated electrochemically using CV (from 0 to 1.6 V) between porphyrin cation (electrogenerated) and Py-POM-Py.	POM core confirmed by CV and EDS	Hybrid POM (Py-POM-Py) is part of the polymer backbone, as it is covalently linked to the porphyrin moieties. However, the copolymerization is not initiated electrochemically by the POM core.	**Photocatalytic recovery of noble metals** / High efficiency in Pt(IV) photoreduction over repeated cycles without catalyst degradation.	[61]

(Continues)

23669808, 2026, 15, Downloaded from https://onlinelibrary.wiley.com/doi/10.1002/smtd.70834 by Spanish Cochrane National Provision (Ministerio de Sanidad), Wiley Online Library on [04/11/2026]. See the Terms and Conditions (https://onlinelibrary.wiley.com/terms-and-conditions) on Wiley Online Library for rules of use; OA articles are governed by the applicable Creative Commons License

TABLE 1 | (Continued)

POM-polymer material	Synthesis procedure	POM characterization	POM arrangement within the hybrid material	Application/efficiency	Refs.
Nanostructured POM-based hybrid polymers (PVW11-PPy and PVW11-PANI) materials	Polymers are synthesized through in situ oxidative polymerization of pyrrole/aniline in the presence of $H_4[PVW_{11}O_{40}]$ using $FeCl_3$ as an oxidizing agent.	POM presence confirmed by PXRD, FTIR, Raman, and elemental mapping	Owing to the high negative charge of PVW_{11}, strong electrostatic interactions are established between the POM anions and the positively charged PPy or PANI chains during electropolymerization (non-covalent entrapment).	**Capacitive energy storage and glucose sensing** / PVW11−PPy: energy density of 49.07 Wh. kg^{-1}, specific capacitance of 405.16 $F.g^{-1}$ at at 1 $A{\cdot}g^{-1}$. Glucose sensitivity: 0.325 $\mu A{\cdot}\mu M^{-1}.cm^{-2}$; LOD: 0.381 µM, LOQ: 1.270 µM (linear range 0.04 – 0.4 mM). PVW11−PANI: energy density of 17.83 Wh. kg^{-1}, specific capacitance of 179.82 $F.g^{-1}$ at at 1 $A{\cdot}g^{-1}$.	[62]
Poly(PW11-ANI) nanofilaments in VMSF (This work)	One-step electropolymerization of covalently functionalized POM-dianiline monomer by CV on bare ITO and within VMSF	POM core confirmed by CV, XPS, FTIR, TEM, EDX, and SEM	POM covalently integrated in the polymer backbone as a bifunctional cross-linker; linear nanofilaments oriented within VMSF mesochannels	**Nitrite reduction** / Onset: −0.1 V vs. Ag/AgCl; Tafel slope: 172 $mV{\cdot}dec^{-1}$ (VMSF) vs. 199 $mV{\cdot}dec^{-1}$ (bulk film); Chronoamperometric stability over 3600 s.	This work

23669608, 2026, 15, Downloaded from https://onlinelibrary.wiley.com/doi/10.1002/smtd.70834 by Spanish Cochrane National Provision (Ministerio de Sanidad), Wiley Online Library on [04/11/2026]. See the Terms and Conditions (https://onlinelibrary.wiley.com/terms-and-conditions) on Wiley Online Library for rules of use; OA articles are governed by the applicable Creative Commons License

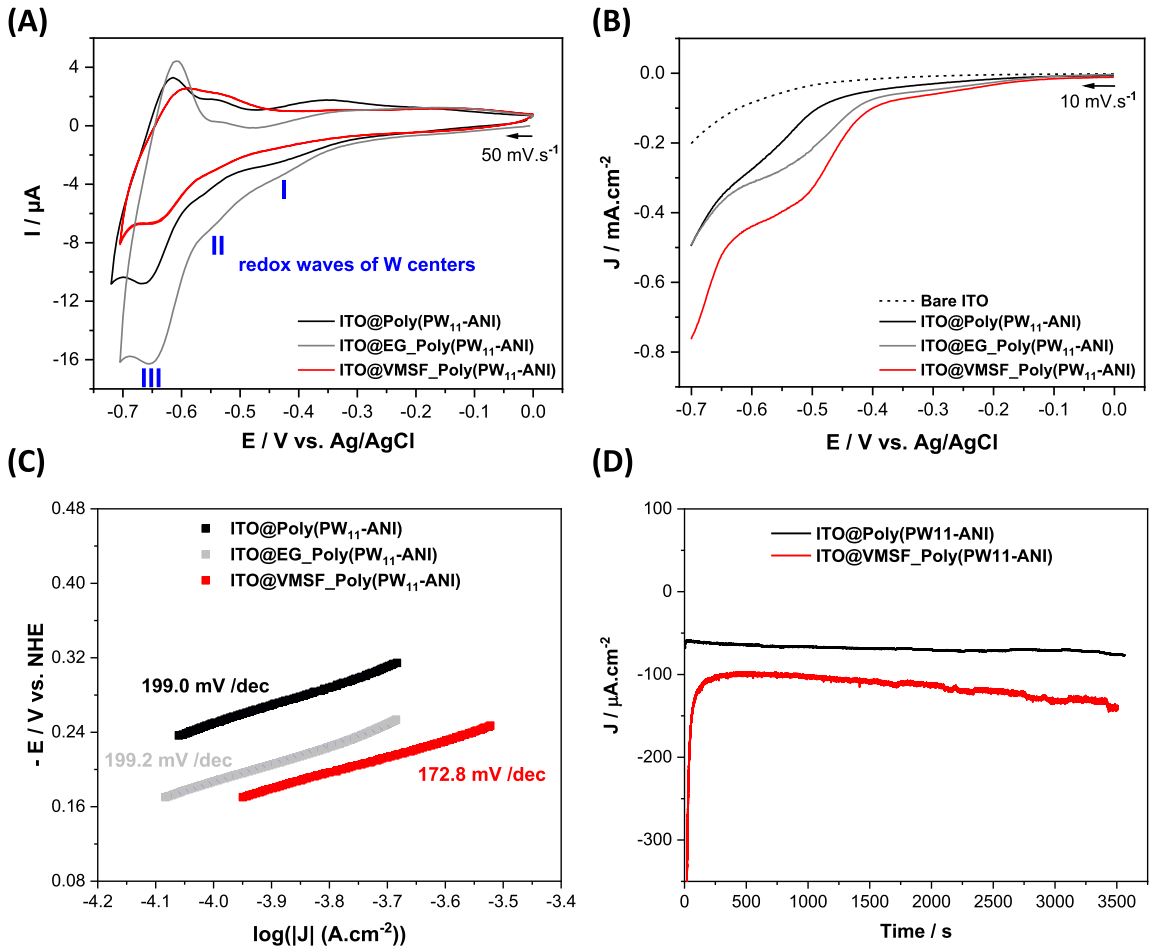


FIGURE 13 | (A) Cyclic voltammograms of poly(PW_{11}-ANI) recorded at 50 mV.s^{-1} in 0.2 M $HClO_4$ in water for the films electropolymerized on bare ITO (ITO@Poly(PW_{11}-ANI), solid black curve), on ITO pre-electrografted with PW_{11}-(ANI)(diaz) (ITO@EG_Poly(PW_{11}-ANI), solid gray curve) and into the oriented mesoporous silica film (ITO@VMSF_Poly(PW_{11}-ANI), solid red curve). (B) Linear sweep voltammetric response of bare ITO electrode (dashed black curve) and the same poly(PW_{11}-ANI) modified electrodes as in (A), recorded at 10 mV.s^{-1} in an aqueous solution (+0.2 M $HClO_4$) containing 8 mM NO_2^-. (C) Tafel plots obtained from the same poly(PW_{11}-ANI) modified electrodes as in (A). (D) Chronoamperometric curves recorded for ITO@Poly(PW_{11}-ANI) (solid black curve) and ITO@VMSF_Poly(PW_{11}-ANI) (solid red curve) at −0.57 V vs. Ag/AgCl during 3600 s in aqueous 0.2 M $HClO_4$ containing 1 mM NO_2^-.

performance by stabilizing the active species and maintaining their electrochemical accessibility over time.

Future work will focus on evaluating the electrocatalytic performance and long-term operational stability of these materials under continuous electrolysis conditions, especially in acidic aqueous environments relevant to practical applications.

Supporting Information

The authors have cited additional references within the Supporting Information [30, 31].

Acknowledgements

The authors acknowledge financial support from the French "Agence Nationale de la Recherche" (N° ANR-20-CE09-0004, POMSIL). The authors thank the spectroscopy and microscopy Service Facility (SMI) of the LCPME for providing access to the XPS.

Conflicts of Interest

The authors declare no conflicts of interest.

Data Availability Statement

The data that support the findings of this study are available from the corresponding author upon reasonable request.

References

1. A. A. A. Aljabali, A. Alkaraki, O. Gammoh, et al., "Design, Structure, and Application of Conductive Polymer Hybrid Materials: A Comprehensive Review of Classification, Fabrication, and Multifunctionality," *RSC Advances* 15 (2025): 27493.

2. K. Namsheer and C. S. Rout, "Conducting Polymers: A Comprehensive Review on Recent Advances in Synthesis, Properties and Applications," *RSC Advances* 11 (2021): 5659–5697.

23669608, 2026, 15, Downloaded from https://onlinelibrary.wiley.com/doi/10.1002/smtd.70834 by Spanish Cochrane National Provision (Ministerio de Sanidad), Wiley Online Library on [04/11/2026]. See the Terms and Conditions (https://onlinelibrary.wiley.com/terms-and-conditions) on Wiley Online Library for rules of use; OA articles are governed by the applicable Creative Commons License

3. S. Kumaravel, E. Kim, B. B. Kale, A. Adhikari, E. Patel, and S. Kundu, "Recent Developments in Conductive Polymer-Based Electro-/Photoelectrocatalytic Materials for Effective Hydrogen/Oxygen Evolution Reactions: A Review," *ChemElectroChem* 9 (2022): 202200724, https://doi.org/10.1002/celc.202200724.

4. M. T. Pope, in *Heteropoly and I. Oxometalates* (Springer, 1983).

5. M. Sadakane and E. Steckhan, "Electrochemical Properties of Polyoxometalates as Electrocatalysts," *Chemical Reviews* 98 (1998): 219–238, https://doi.org/10.1021/cr960403a.

6. H. N. Miras, J. Yan, D.-L. Long, and L. Cronin, "Engineering Polyoxometalates With Emergent Properties," *Chemical Society Reviews* 41 (2012): 7403–7430, https://doi.org/10.1039/c2cs35190k.

7. I. A. Weinstock, R. E. Schreiber, and R. Neumann, "Dioxygen in Polyoxometalate Mediated Reactions," *Chemical Reviews* 118 (2018): 2680–2717.

8. K. Suzuki, N. Mizuno, and K. Yamaguchi, "Polyoxometalate Photocatalysis for Liquid-Phase Selective Organic Functional Group Transformations," *ACS Catalysis* 8 (2018): 10809–10825, https://doi.org/10.1021/acscatal.8b03498.

9. A. Misra, K. Kozma, C. Streb, and M. Nyman, "Beyond Charge Balance: Counter-Cations in Polyoxometalate Chemistry," *Angewandte Chemie International Edition* 59 (2020): 596–612, https://doi.org/10.1002/anie.201905600.

10. G. Bidan, E. M. Genies, and M. Lapkowski, "Modification of Polyaniline Films With Heteropolyanions: Electrocatalytic Reduction of Oxygen and Protons," *Journal of Chemical Society* 5 (1988): 533–535.

11. G. Bidan, M. Lapkowski, and J. P. Travers, "Hybridization of Various Conducting Polymers With Heteropoyyanious: Conductivity, Electrochemical and Electrocatalytic Properties," *Synthetic Metals* 28 (1989): 113–120, https://doi.org/10.1016/0379-6779(89)90507-9.

12. B. Keita, D. Bouaziz, and L. Nadjo, "Strategies for Entrapping Oxometalates in Polymeric Matrices," *Journal of Electroanalytical Chemistry and Interfacial Electrochemistry* 255 (1988): 307–313, https://doi.org/10.1016/0022-0728(88)80023-8.

13. W. Baoxing, D. Fayi, and D. Shaojun, "The Preparation of Electrodes Modified With Isopolymolybdic Acid + Polyaniline Film and Its Catalytic Effects on Chlorate Ions," *Journal of Electroanalytical Chemistry* 353: 43–55, https://doi.org/10.1016/0022-0728(93)80285-P.

14. B. Wang and S. Dong, "Electrochemical Study of Isopoly- and Heteropoly-Oxometallates Film Modified Microelectrodes—Part 3. Further Study of Electrode Process of Isopolymolybdic Anion Doped in Polyaniline Film," *Electrochimica Acta* 38 (1993): 1029–1035, https://doi.org/10.1016/0013-4686(93)87023-7.

15. M. Lira-Cantú and P. Gómez-Romero, "Electrochemical and Chemical Syntheses of the Hybrid Organic–Inorganic Electroactive Material Formed by Phosphomolybdate and Polyaniline. Application as Cation-Insertion Electrodes," *Chemistry of Materials* 10 (1998): 698–704, https://doi.org/10.1021/cm970107u.

16. P. Gómez-Romero and M. Lira-Cantú, "Hybrid Organic-Inorganic Electrodes: The Molecular Material Formed between Polypyrrole and the Phosphomolybdate Anion," *Advanced Materials* 9 (1997): 144–147, https://doi.org/10.1002/adma.19970090210.

17. P. Gómez-Romero, N. Casañ-Pastor, and M. Lira-Cantú, "Chemical Polymerization of Polyaniline and Polypyrrole by Phosphomolybdic Acid: In Situ Formation of Hybrid Organic–Inorganic Materials," *Solid State Ionics* 101-103 (1997): 875–880.

18. G. M. Suppes, B. A. Deore, and M. S. Freund, "Porous Conducting Polymer/Heteropolyoxometalate Hybrid Material for Electrochemical Supercapacitor Applications," *Langmuir* 24 (2008): 1064–1069, https://doi.org/10.1021/la702837j.

19. S. Herrmann, C. Ritchie, and C. Streb, "Polyoxometalate—Conductive Polymer Composites for Energy Conversion, Energy Storage and Nanostructured Sensors," *Dalton Transactions* 44 (2015): 7092–7104, https://doi.org/10.1039/C4DT03763D.

20. J.-H. Kruse, M. Langer, I. Romanenko, et al., "Polyoxometalate-Soft Matter Composite Materials: Design Strategies, Applications, and Future Directions," *Advanced Functional Materials* 32 (2022): 2208428, https://doi.org/10.1002/adfm.202208428.

21. M. Góral, T. McCormac, E. Dempsey, and A. F. Murphy, "Development of Electrocatalytic Hybrid Film Based on Conducting Polypyrrole Heteropolyanion," *Journal of Electroanalytical Chemistry* 952 (2024): 117848.

22. M. Blasco-Ahicart, J. Soriano-López, and J. R. Galán-Mascarós, "Conducting Organic Polymer With Embedded Polyoxometalate Catalysts for Water Splitting," *ChemElectroChem* 4 (2017): 3296–3301.

23. W. Qi and L. Wu, "Polyoxometalate/Polymer Hybrid Materials: Fabrication and Properties," *Polymer International* 58 (2009): 1217–1225, https://doi.org/10.1002/pi.2654.

24. A. Dolbecq, E. Dumas, C. R. Mayer, and P. Mialane, "Hybrid Organic–Inorganic Polyoxometalate Compounds: From Structural Diversity to Applications," *Chemical Reviews* 110 (2010): 6009–6048, https://doi.org/10.1021/cr1000578.

25. T. Iftikhar and H. Mu, "Covalent Organic–Inorganic Polyoxometalate Hybrids in Catalysis," *Frontiers in Chemistry* 12 (2024): 1447623, https://doi.org/10.3389/fchem.2024.1447623.

26. A. V. Anyushin, A. Kondinski, and T. N. Parac-Vogt, "Hybrid Polyoxometalates as Post-Functionalization Platforms: From Fundamentals to Emerging Applications," *Chemical Society Reviews* 49 (2020): 382–432, https://doi.org/10.1039/C8CS00854J.

27. H. Zhang, W. L. Zhao, H. Li, et al., "Latest Progress in Covalently Modified Polyoxometalates-Based Molecular Assemblies and Advanced Materials," *Polyoxometalates* 1 (2022): 9140011, https://doi.org/10.26599/POM.2022.9140011.

28. J. M. Cameron, G. Guillemot, T. Galambos, et al., "Supramolecular Assemblies of Organo-Functionalized Hybrid Polyoxometalates: From Functional Building Blocks to Hierarchical Nanomaterials," *Chemical Society Reviews* 51 (2022): 293–328, https://doi.org/10.1039/D1CS00832C.

29. C. Priyanka, Y. N. Sudhakar, G. T. Mahesha, N. Gi, and K. P. D. Vishnu, "Polyoxometalate-Based Hybrid Supercapacitors: Advances, Challenges, and Future Prospects in Sustainable Energy Storage," *Chemical Engineering Journal Advances* 24 (2025): 100908.

30. R. Salles, W. C. Poh, M. Laurans, et al., "Covalent Shaping of Polyoxometalate Molecular Films onto ITO Electrodes for Charge Trapping Induced Resistive Switching," *Inorganic Chemistry Frontiers* 11 (2024): 255–268, https://doi.org/10.1039/D3QI01761C.

31. S. A. Alshehri, A. Al-Yasari, F. Marken, and J. Fielden, "Covalently Linked Polyoxometalate–Polypyrrole Hybrids: Electropolymer Materials With Dual-Mode Enhanced Capacitive Energy Storage," *Macromolecules* 53 (2020): 11120–11129, https://doi.org/10.1021/acs.macromol.0c02354.

32. B. Matt, S. Renaudineau, L.-M. Chamoreau, C. Afonso, G. Izzet, and A. Proust, "Hybrid Polyoxometalates: Keggin and Dawson Silyl Derivatives as Versatile Platforms," *Journal of Organic Chemistry* 76 (2011): 3107–3112, https://doi.org/10.1021/jo102546v.

33. A. M. P. Hussain and A. Kumar, "Electrochemical Synthesis and Characterization of Chloride Doped Polyaniline," *Bulletin of Materials Science* 26 (2003): 329–334, https://doi.org/10.1007/BF02707455.

34. M. M. Gvozdenovic´, B. Z. Jugovic´, J. S. Stevanovic´, T. L. Trišovic´, and B. N. Grgur, "*Electrochemical Polymerization of Aniline*," ed. E. Schab-Balcerzak, (IntechOpen, 2011), 77–96.

35. A. J. Bard and L. R. Faulkner, in *Electrochemical Methods: Fundamentals and Applications*, 2nd ed. (Wiley, 2001).

36. E. M. Geniès, A. Boyle, M. Lapkowski, and C. Tsintavis, "Polyaniline: A Historical Survey," *Synthetic Metals* 136 (1990): 182.

23669608, 2026, 15, Downloaded from https://onlinelibrary.wiley.com/doi/10.1002/smtd.70834 by Spanish Cochrane National Provision (Ministerio de Sanidad), Wiley Online Library on [04/11/2026]. See the Terms and Conditions (https://onlinelibrary.wiley.com/terms-and-conditions) on Wiley Online Library for rules of use; OA articles are governed by the applicable Creative Commons License

37. W. Ullah, G. Herzog, N. Vilà, and A. Walcarius, "Electrografting and Electropolymerization of Nanoarrays of PANI Filaments Through Silica Mesochannels," *Electrochemistry Communications* 122 (2021): 106896, https://doi.org/10.1016/j.elecom.2020.106896.

38. N. Vilà, L. Nguyen, J. C. Lacroix, X. Sun, A. Walcarius, and I. M. Mbomekallé, "Assessing the Influence of Confinement on the Stability of Polyoxometalate-functionalized Surfaces: A Soft Sequential Immobilization Approach for Electrochromic Devices," *ACS Applied Materials & Interfaces* 16 (2024): 26521–26536, https://doi.org/10.1021/acsami.4c01859.

39. R. Kanaan, E. André, M. Dossot, A. Walcarius, and N. Vilà, "Electropolymerization Mechanism of Aminophenyl-bis(terpyridine) Metal Complexes Featuring Electrochromic Properties," *Langmuir* 41 (2025): 30276–30290, https://doi.org/10.1021/acs.langmuir.5c03774.

40. C. Rinfray, G. Izzet, J. Pinson, et al., "Electrografting of Diazonium-Functionalized Polyoxometalates: Synthesis, Immobilization and Electron-Transfer Characterization From Glassy Carbon," *Chemistry—A European Journal* 19 (2013): 13838–13846, https://doi.org/10.1002/chem.201302304.

41. A. A. Salem and B. N. Grgur, "The Influence of the Polyaniline Initial Oxidation States on the Corrosion of Steel With Composite Coatings," *Progress in Organic Coatings* 119 (2018): 138–144, https://doi.org/10.1016/j.porgcoat.2018.02.032.

42. J. E. Albuquerque, L. H. C. Mattoso, R. M. Faria, J. G. Masters, and A. G. MacDiarmid, "Study of the Interconversion of Polyaniline Oxidation States by Optical Absorption Spectroscopy," *Synthetic Metals* 146 (2004): 1–10, https://doi.org/10.1016/j.synthmet.2004.05.019.

43. M. Guzel, Y. Torlak, H. Choi, and M. Ak, "Designed Hybrid Organic–Inorganic Nanocomposite Film Based on Synergistic Effect of Conducting Polymer and Keggin Type Polyoxometalate Clusters," *Materials Research Bulletin* 167 (2023): 112406, https://doi.org/10.1016/j.materresbull.2023.112406.

44. N. Biyikli, I. Kimukin, B. Butun, O. Aytur, and E. Ozbay, "ITO-Schottky Photodiodes for High-Performance Detection in the UV–IR Spectrum," *IEEE Journal of Selected Topics in Quantum Electronics* 10 (2004): 759–765, https://doi.org/10.1109/JSTQE.2004.833977.

45. M. G. Han and S. S. Im, "X-Ray Photoelectron Spectroscopy Study of Electrically Conducting Polyaniline/Polyimide Blends," *Polymer* 41 (2000): 3253–3262, https://doi.org/10.1016/S0032-3861(99)00531-5.

46. W. Ullah, G. Herzog, N. Vilà, and A. Walcarius, "Polyaniline Nanowire Arrays Generated Through Oriented Mesoporous Silica Films: Effect of Pore Size and Spectroelectrochemical Response," *Faraday Discussions* 233 (2022): 77–99, https://doi.org/10.1039/D1FD00034A.

47. S.-X. Guo, A. W. A. Mariotti, C. Schlipf, A. M. Bond, and A. G. Wedd, "Investigation of the Pronounced Medium Effects Observed in the Voltammetry of the Highly Charged Lacunary Anions [α-SiW 11 O 39] 8- and [α-PW 11 O 39] 7-," *Inorganic Chemistry* 45 (2006): 8563–8574, https://doi.org/10.1021/ic061081o.

48. K. G. Neo, E. T. Kang, and K. L. Tan, "Comparative Study on the Structural Changes in Leucoemeraldine and Emeraldine Base Upon Doping by Perchlorate," *Journal of Polymer Science A* 29 (1991): 759–766.

49. L. Galleni, A. Meulemans, F. S. Sajjadian, et al., "Peak Broadening in Photoelectron Spectroscopy of Amorphous Polymers: The Leading Role of the Electrostatic Landscape," *Journal of Physical Chemistry Letters* 15 (2024): 834–839, https://doi.org/10.1021/acs.jpclett.3c02640.

50. X. B. Han, Y. G. Li, Z. M. Zhang, H. Q. Tan, Y. Lu, and E. B. Wang, "Polyoxometalate-Based Nickel Clusters as Visible Light-Driven Water Oxidation Catalysts," *Journal of the American Chemical Society* 137 (2015): 5486–5493, https://doi.org/10.1021/jacs.5b01329.

51. Y. Zhou, F. Bihl, A. Bonnefont, C. Boudon, L. Ruhlmann, and V. Badets, "Selectivity and Efficiency of Nitrite Electroreduction Catalyzed by a Series of Keggin Polyoxometalates," *Journal of Catalysis* 405 (2022): 212–223, https://doi.org/10.1016/j.jcat.2021.11.037.

52. Y. Zhou, J. Sun, S. Gallet, et al., "Nitrite Electroreduction Enhanced by Hybrid Compounds of Keggin Polyoxometalates and 1-Butyl-3-vinylimidazolium," *ChemCatChem* 16 (2024): 202400226.

53. Y. Shahaf, T. K. Slot, S. Avidan, J. E. Dick, and D. Eisenberg, "Buffer Effects on Nitrite Reduction Electrocatalysis," *ACS Catalysis* 15, no. 9 (2025): 7254–7262.

54. D. De, J. D. Englehardt, and E. E. Kalu, "Cyclic Voltammetric Studies of Nitrate and Nitrite Ion Reduction at the Surface of Iridium-Modified Carbon Fiber Electrode," *Journal of the Electrochemical Society* 147, no. 11 (2000): 4224, https://doi.org/10.1149/1.1394045.

55. J. Wu, S. Wu, and W. Sun, "Electropolymerization and Application of Polyoxometalate-Doped Polypyrrole Film Electrodes in Dye-Sensitized Solar Cells," *Electrochemistry Communications* 122 (2021): 106879, https://doi.org/10.1016/j.elecom.2020.106879.

56. M. Yu, S. Rong, X. Wang, et al., "Preparation and Application of Keggin Polyoxometalate-Based 3D Coordination Polymer Materials as Supercapacitors and Amperometric Sensors," *ChemNanoMat* 7, no. 3 (2021): 299–306.

57. S. A. Alshehri, A. Al-Yasari, F. Marken, and J. Fielden, "Covalently Linked Polyoxometalate–Polypyrrole Hybrids: Electropolymer Materials With Dual-Mode Enhanced Capacitive Energy Storage," *Macromolecules* 53, no. 24 (2020): 11120–11129.

58. B. R. Biradar, N. Thathron, P. P. Das, and S. S. Mal, "Pseudocapacitive Effects of Polyoxometalate Implanted on Graphene Oxide Matrix with Polypyrrole for Symmetric Supercapacitor Applications," *Journal of Electroanalytical Chemistry* 960 (2024): 118192, https://doi.org/10.1016/j.jelechem.2024.118192.

59. A. K. Rajan, I. Sakthinathan, and T. McCormac, "Electrochemical Characterisation of $\{Ni_{14}SiW_9ale_7\}$ (ale = alendronate)-Doped PEDOT Hybrid Polyoxometalate Film," *Journal of Electroanalytical Chemistry* 996 (2025): 119322, https://doi.org/10.1016/j.jelechem.2025.119322.

60. Y. Torlak, R. Ayranci, and M. Ak, "In Situ Electrochemical Production of Metal-Organic Hybrid Composite Film From Nickel Containing Polyoxometalate and 3,4-Ethylenedioxy-thiophene for Sensor Application," *Electroanalysis* 33, no. 9 (2021): 2025–2032.

61. Z. Huo, B. Akhsassi, J. Yu, et al., "Photocatalytic Recovery of Noble Metals by Covalent Silyl Polyoxophosphotungstate–Porphyrin Copolymers," *Inorganic Chemistry* 64, no. 7 (2025): 3371–3383, https://doi.org/10.1021/acs.inorgchem.4c04890.

62. M. A. Puniyanikkottil and S. S. Mal, "Polyoxometalate Integrated With Conducting Polymer Nanocomposites for Supercapacitor and Biological Sensor Applications," *Inorganic Chemistry* 64, no. 16 (2025): 8222–8237, https://doi.org/10.1021/acs.inorgchem.5c00473.

Supporting Information

Additional supporting information can be found online in the Supporting Information section.

Supporting File: smtd70834-sup-0001-SuppMat.docx.

23669608, 2026, 15, Downloaded from https://onlinelibrary.wiley.com/doi/10.1002/smtd.70834 by Spanish Cochrane National Provision (Ministerio de Sanidad), Wiley Online Library on [04/11/2026]. See the Terms and Conditions (https://onlinelibrary.wiley.com/terms-and-conditions) on Wiley Online Library for rules of use; OA articles are governed by the applicable Creative Commons License